

# An accurate, robust, and efficient finite element framework for anisotropic, nearly and fully incompressible elasticity

Elias Karabelas<sup>a</sup>, Matthias A. F. Gsell<sup>b</sup>, Gernot Plank<sup>b,c</sup>, Gundolf Haase<sup>a,c</sup>, Christoph M. Augustin<sup>b,\*</sup>

<sup>a</sup>*Institute for Mathematics and Scientific Computing, Karl-Franzens-University Graz, Graz, Austria*

<sup>b</sup>*Gottfried Schatz Research Center: Division of Biophysics, Medical University of Graz, Graz, Austria*

<sup>c</sup>*BioTechMed-Graz, Graz, Austria*

---

## Abstract

Fiber-reinforced soft biological tissues are typically modeled as hyperelastic, anisotropic, and nearly incompressible materials. To enforce incompressibility a multiplicative split of the deformation gradient into a volumetric and an isochoric part is a very common approach. However, due to the high stiffness of anisotropic materials in the preferred directions, the finite element analysis of such problems often suffers from severe locking effects and numerical instabilities. In this paper, we present novel methods to overcome locking phenomena for anisotropic materials using stabilized P1-P1 elements. We introduce different stabilization techniques and demonstrate the high robustness and computational efficiency of the chosen methods. In several benchmark problems we compare the approach to standard linear elements and show the accuracy and versatility of the methods to simulate anisotropic, nearly and fully incompressible materials. We are convinced that this numerical framework offers the possibility to accelerate accurate simulations of biological tissues, enabling patient-specific parameterization studies, which require numerous forward simulations.

*Keywords:* Stabilized finite element methods, anisotropic materials, quasi-incompressibility, soft biological tissues, cardiac electromechanics

---

## 1. Introduction

Computer models of biological tissues, e.g., the simulation of vessel mechanics or cardiac electro-mechanics (EM), aid in understanding the biomechanical function of the organs and show promise to be a powerful tool for predicting therapeutic responses. Advanced applications include the simulation of growth and remodeling processes occurring in the failing heart or arteries [1, 2, 3, 4] as well as rupture risk assessment in arterial aneurysms [5, 6]. Here, predictions of *in-silico* models are often based on the computation of local stresses, hence, an accurate computation of strain and stress is indispensable to build confidence in simulation outcomes. Additionally, high computational efficiency and excellent strong scaling properties are crucial to perform simulations with highly-resolved, complex, or heterogeneous geometries; to facilitate model personalization using a large number of forward simulations; and to simulate tissue behavior over a broad range of experimental protocols and extended observation periods.

*In-silico* models of cardiac tissue and vessel walls are typically based on the theory of hyperelasticity and properties of soft tissues include a nonlinear relationship between stress and strain with large deformations and a nearly-incompressible, anisotropic materials [7, 8, 9]. Commonly, the resulting non-linear formulations are approximately solved using a finite element (FE) approach [10, 11, 12, 13]. However, volumetric locking phenomena that are resulting in ill-conditioned global stiffness matrices are frequently encountered. In fact, this one of the classical problems of modeling nearly incompressible hyperelasticity [14, 15, 16]. Locking, often completely invalidating FE solutions, is in particular prevalent for fiber-reinforced soft biological tissues due to a high stiffness in the preferred fiber directions and thus extensively studied in recent publications [17, 18, 19, 20].

---

\*Address correspondence to Christoph M. Augustin, Gottfried Schatz Research Center: Division of Biophysics, Medical University of Graz, Neue Stiftingtalstrasse 6/IV, Graz 8010, Austria. Email: christoph.augustin@medunigraz.at

Typically, the modeling of (nearly) incompressible elastic materials involves a split of the deformation gradient into a volumetric and an isochoric part [21]. Here, locking phenomena are very common when using unstable approximation pairs such as Q1-P0 or P1-P0 elements, i.e., when linear shape functions are the choice to approximate the displacement field  $\mathbf{u}$  and the hydrostatic pressure  $p$  is statically condensed from the system of equations on the element-level. It is well known that in such cases solution algorithms are likely to show very low convergence rates, and that variables of interest such as stresses can be inaccurate [18].

To some degree locking problems in anisotropic hyperelasticity for these simple elements can be reduced by using augmented Lagrangian methods [22, 23], formulations with an unsplit deformation gradient for the anisotropic contribution [24, 25], and methods with simplified kinematics for the anisotropic contributions [26]. Another possibility to obtain more accurate results is the use of higher order polynomials to approximate the displacement [27, 28, 29, 30]. However, the incompressibility constraint is still modeled by a penalty formulation, hence, volumetric locking may still be an issue and the modeling of fully incompressible materials is not possible. Additionally, already for quadratic ansatz functions the considerable larger amount of degrees of freedom increases computational cost significantly.

A more sophisticated approach – also allowing the modeling of fully incompressible materials – is the reformulation of the underlying equations into a saddle point problem by introducing the hydrostatic pressure  $p$  as an additional unknown to the system. Here, from mathematical theory, approximation pairs for  $\mathbf{u}$  and  $p$  have to fulfill the Ladyzhenskaya–Babuška–Brezzi (LBB) or *inf-sup* conditions [31, 32, 33] to guarantee stability. A popular choice are quadratic ansatz functions for the displacement and linear ansatz functions for the pressure, i.e., the Taylor–Hood element [34, 35]. Though stable, this element leads to a vast increase in degrees of freedom and consequently a high computational burden; especially for applied problems in the field of tissue mechanics with highly resolved geometries.

A computationally more favorable choice are equal order pairs with a stabilization, widely used for linear and isotropic elasticity [36, 37, 38, 39, 40, 41, 42]. Yet, their extension to non-linear, anisotropic problems is challenging [43, 44, 26]. In the specific case of modeling biological tissues Hu–Washizu-based formulations are often used, e.g., [45, 46, 47, 48]. However, especially for problems undergoing large strains, this mixed three field approach shows limited performance and robustness [26].

As our results suggest, a very promising and efficient stabilization approach for nearly incompressible, anisotropic elasticity problems is a variant of the MINI element [49], originally established for computational fluid dynamics problems. This element is modified for the application of incompressible hyperelasticity and a bubble function is included in the space of displacements. To improve efficiency, the support of this bubble can be eliminated from the system of equation using static condensation. First uses of MINI elements have been reported [50, 51] though still using a piecewise constant ansatz for the hydrostatic pressure. Even more efficient and notably simple to implement is a pressure projection method originally introduced for the Stokes problem [52]. To the best of our knowledge the here proposed methods were not yet used in this form for anisotropic and nearly incompressible materials.

A big advantage of both stabilization techniques is that they do not rely on artificial stabilization parameters that may influence the numerical solution. We illustrate in different benchmarks that the same setting can be used for a large variety of tissue mechanics problems allowing for a one-for-all approach. By comparing to literature we show that our methods are suitable to compute accurate strain and stress fields and outperform existing contributions in terms of efficiency.

The paper is outlined as follows: in [Section 2](#) we recall the mathematical background of modeling anisotropic, nearly incompressible elasticity and introduce the theoretical framework of our stabilization techniques. Subsequently, [Section 3](#) documents three benchmark problems to show the applicability of the stabilized P1-P1 elements in different scenarios. For each benchmark we give a detailed problem description and discuss results and computational efficiency by comparing to the literature and analyzing strong-scaling properties.

To show the usefulness of the presented methods to clinically relevant problems, we present a 3D EM model of the heart that is coupled to a 0D model of blood flow. This constitutes the most complete model of cardiac EM in the literature to date as all components, i.e., electrophysiology, cellular dynamics, active stress, passive tissue mechanics, pre- and afterload, are based on physiological, state-of-the-art models from the literature. Finally, [Section 4](#) concludes the paper with a brief summary and all required equations to implement the methods in a software framework are given in the Appendix.

## 2. Methodology

### 2.1. Almost Incompressible Nonlinear Elasticity

Let  $\Omega_0 \subset \mathbb{R}^3$  denote the reference configuration and let  $\Omega_t \subset \mathbb{R}^3$  denote the current configuration of the domain of interest. Assume that the boundary of  $\Omega_0$  is decomposed into  $\partial\Omega_0 = \Gamma_{D,0} \cup \Gamma_{N,0}$  with  $|\Gamma_{D,0}| > 0$ . Here,  $\Gamma_{D,0}$  describes the Dirichlet part of the boundary and  $\Gamma_{N,0}$  describes the Neumann part of the boundary, respectively. Further, let  $\mathbf{N}$  be the unit outward normal on  $\partial\Omega_0$ . The nonlinear mapping  $\phi: \mathbf{X} \in \Omega_0 \rightarrow \mathbf{x} \in \Omega_t$ , defined by  $\phi := \mathbf{X} + \mathbf{u}(\mathbf{X}, t)$ , with displacement  $\mathbf{u}$ , maps points in the reference configuration to points in the current configuration. Following standard notation, we introduce the *deformation gradient*  $\mathbf{F}$ , the Jacobian  $J$ , and the *left Cauchy-Green tensor*  $\mathbf{C}$  as

$$\mathbf{F} := \text{Grad } \phi = \mathbf{I} + \text{Grad } \mathbf{u}, \quad J := \det(\mathbf{F}), \quad \mathbf{C} := \mathbf{F}^\top \mathbf{F}.$$

Here,  $\text{Grad}(\bullet)$  denotes the gradient with respect to the reference coordinates  $\mathbf{X} \in \Omega_0$ . The displacement field  $\mathbf{u}$  is sought as infimizer of the functional

$$\begin{aligned} \Pi^{\text{tot}}(\mathbf{u}) &:= \Pi(\mathbf{u}) + \Pi^{\text{ext}}(\mathbf{u}), \\ \Pi(\mathbf{u}) &:= \int_{\Omega_0} \Psi(\mathbf{F}(\mathbf{u})) \, d\mathbf{X}, \\ \Pi^{\text{ext}}(\mathbf{u}) &:= -\rho_0 \int_{\Omega_0} \mathbf{f}(\mathbf{X}) \cdot \mathbf{u} \, d\mathbf{X} - \int_{\Gamma_{N,0}} \mathbf{h}(\mathbf{u}) \cdot \mathbf{u} \, ds_{\mathbf{X}}, \end{aligned} \quad (1)$$

over all admissible fields  $\mathbf{u}$  with  $\mathbf{u} = \mathbf{g}_D$  on  $\Gamma_{D,0}$ , where,  $\Psi$  denotes the strain energy function;  $\rho_0$  denotes the material density in reference configuration;  $\mathbf{f}$  denotes a volumetric body force;  $\mathbf{g}_D$  denotes a given boundary displacement; and  $\mathbf{h}$  denotes a given follower surface traction defined as

$$\mathbf{h}(\mathbf{u}) := -p_{\text{ext}} J(\mathbf{u}) \mathbf{F}^{-\top}(\mathbf{u}) \mathbf{N},$$

with giving external load  $p_{\text{ext}} > 0$ . For ease of presentation it is assumed that  $\rho_0$  is constant and  $\mathbf{f}$ , and  $\mathbf{g}_D$  do not depend on  $\mathbf{u}$ . Existence of infimizers is, under suitable assumptions, guaranteed by the pioneering works of Ball, see [53] and [54] for the case of follower loads.

In this study, we consider nearly incompressible materials, meaning that  $J \approx 1$ . A possibility to model this behavior was originally proposed by [21] using a split of the deformation gradient  $\mathbf{F}$  such that

$$\mathbf{F} = \mathbf{F}_{\text{vol}} \bar{\mathbf{F}}. \quad (2)$$

Here,  $\mathbf{F}_{\text{vol}}$  describes the volumetric change while  $\bar{\mathbf{F}}$  describes the isochoric change. By setting  $\mathbf{F}_{\text{vol}} := J^{\frac{1}{3}} \mathbf{I}$  and  $\bar{\mathbf{F}} := J^{-\frac{1}{3}} \mathbf{F}$  we get  $\det(\bar{\mathbf{F}}) = 1$  and  $\det(\mathbf{F}_{\text{vol}}) = J$ . Analogously, by setting  $\mathbf{C}_{\text{vol}} := J^{\frac{2}{3}} \mathbf{I}$  and  $\bar{\mathbf{C}} := J^{-\frac{2}{3}} \mathbf{C}$ , we have  $\mathbf{C} = \mathbf{C}_{\text{vol}} \bar{\mathbf{C}}$ . Assuming a hyperelastic material, the Flory split also postulates an additive decomposition of the strain energy function

$$\Psi = \Psi(\mathbf{C}) = U(J) + \bar{\Psi}(\bar{\mathbf{C}}). \quad (3)$$

The function  $U(J)$  will be used in the form

$$U(J) := \frac{\kappa}{2} \Theta(J)^2$$

where  $\kappa$  denotes the *bulk modulus*. In the literature many different choices for the functions  $\Theta(J)$  are proposed, see e.g [55, 56, 57] for examples and related discussion. For studying also the limit case  $\kappa \rightarrow \infty$  we will consider a reformulation of Equation (1) as perturbed Lagrangian-multiplier functional, see [58, 59, 60, 61] for details. Introducing the hydrostatic pressure  $p$  we seek infimizers  $(\mathbf{u}, p) \in V_{\mathbf{g}_D} \times Q$  of

$$\begin{aligned} \Pi^{\text{tot}}(\mathbf{u}, p) &:= \Pi^{\text{PL}}(\mathbf{u}, p) + \Pi^{\text{ext}}(\mathbf{u}), \\ \Pi^{\text{PL}}(\mathbf{u}, p) &:= \int_{\Omega_0} \bar{\Psi}(\bar{\mathbf{C}}) + p\Theta(J(\mathbf{u})) - \frac{1}{2\kappa} p^2 \, d\mathbf{X}. \end{aligned} \quad (4)$$

To guarantee well-definedness, we assume that

$$V_{\mathbf{g}_D} := \{ \mathbf{v} \in [H^1(\Omega_0)]^3 : \mathbf{v}|_{\Gamma_{D,0}} = \mathbf{g}_D \},$$

with  $H_0^1(\Omega_0)$  being the standard Sobolev space of square integrable functions having a square integrable gradient, and  $Q = L^2(\Omega_0)$ . For a more in-depth discussion we refer to [53, 54]. To solve for infimizers of Equation (4) we calculate the variations with respect to  $\mathbf{v}$  and  $q$ . This results in the following non-linear variational problem, find  $(\mathbf{u}, p) \in V_{\mathbf{g}_D} \times Q$  such that

$$R_{\text{vol}}(\mathbf{u}, p; \mathbf{v}) = 0, \quad (5)$$

$$R_{\text{inc}}(\mathbf{u}, p; q) = 0, \quad (6)$$

for all  $(\mathbf{v}, q) \in V_0 \times Q$ . Here,

$$R_{\text{vol}}(\mathbf{u}, p; \mathbf{v}) := a_{\text{isc}}(\mathbf{u}; \mathbf{v}) + a_{\text{vol}}(\mathbf{u}; \mathbf{v}) - l_{\text{follow}}(\mathbf{u}, p_{\text{ext}}; \mathbf{v}),$$

$$R_{\text{inc}}(\mathbf{u}, p; \mathbf{v}) := b_{\text{vol}}(\mathbf{u}; q) - c(p, q),$$

where

$$a_{\text{isc}}(\mathbf{u}; \mathbf{v}) := \int_{\Omega_0} \mathbf{S}_{\text{isc}}(\mathbf{u}) : \boldsymbol{\Sigma}(\mathbf{u}, \mathbf{v}) \, d\mathbf{X}, \quad a_{\text{vol}}(\mathbf{u}, p; \mathbf{v}) := \int_{\Omega_0} p \mathbf{S}_{\text{vol}}(\mathbf{u}) : \boldsymbol{\Sigma}(\mathbf{u}, \mathbf{v}) \, d\mathbf{X},$$

$$b_{\text{vol}}(\mathbf{u}; q) := \int_{\Omega_0} \Theta(J(\mathbf{u})) q \, d\mathbf{X}, \quad c(p, q) := \frac{1}{\kappa} \int_{\Omega_0} p q \, d\mathbf{X},$$

$$l_{\text{follow}}(\mathbf{u}, p_{\text{ext}}; \mathbf{v}) := -p_{\text{ext}} \int_{\Gamma_N} J(\mathbf{u}) \mathbf{F}^{-\top} \mathbf{N} \cdot \mathbf{v} \, ds_{\mathbf{X}},$$

with  $\boldsymbol{\Sigma}(\mathbf{u}, \mathbf{v}) := \text{sym}(\mathbf{F}^\top(\mathbf{u}) \text{Grad } \mathbf{v})$ . Components of the second Piola–Kirchhoff stress tensor

$$\mathbf{S}_{\text{tot}} = \mathbf{S}_{\text{vol}} + \mathbf{S}_{\text{isc}} \quad (7)$$

are computed as

$$\mathbf{S}_{\text{isc}} := J^{-\frac{2}{3}} \text{Dev}(\bar{\mathbf{S}}), \quad \bar{\mathbf{S}} := \frac{\partial \bar{\Psi}(\bar{\mathbf{C}})}{\partial \bar{\mathbf{C}}} \quad \mathbf{S}_{\text{vol}} := \pi(J) \mathbf{C}^{-1}, \quad \pi(J) := J \Theta'(J).$$

When modeling electrically active tissue, we consider an additive decomposition of the isochoric part of the stress tensor. The total stress tensor is now given by the additive decomposition

$$\mathbf{S}_{\text{tot}} = \mathbf{S}_{\text{a}} + \mathbf{S}_{\text{p}} = \mathbf{S}_{\text{a}} + 2 \frac{\partial \Psi(\mathbf{C})}{\partial \mathbf{C}}. \quad (8)$$

To simulate the effect of the circulatory system, these equations are coupled to a 0D lumped model as in [62]. The corresponding nonlinear variational problem reads as find  $(\mathbf{u}, p) \in V_{\mathbf{g}_D} \times Q$  and  $\underline{p}_{\text{CAV}} \in \mathbb{R}^{n_{\text{CAV}}}$  such that

$$R_{\text{vol}}(\mathbf{u}, p, \underline{p}_{\text{CAV}}; \mathbf{v}) = 0, \quad (9)$$

$$R_{\text{inc}}(\mathbf{u}, p; q) = 0, \quad (10)$$

$$R_{\text{CAV},i}(\mathbf{u}, p_{\text{CAV},i}) = 0, \quad (11)$$

for all  $(\mathbf{v}, q) \in V_0 \times Q$ , and  $i = 1, \dots, n_{\text{CAV}}$ . Here, the variations read as

$$R_{\text{vol}}(\mathbf{u}, p, \underline{p}_{\text{CAV}}; \mathbf{v}) := a_{\text{isc}}(\mathbf{u}; \mathbf{v}) + a_{\text{vol}}(\mathbf{u}; \mathbf{v}) + \sum_{i=1}^{n_{\text{CAV}}} l_{\text{follower}}(\mathbf{u}, p_{\text{CAV},i}; \mathbf{v}), \quad (12)$$

$$R_{\text{inc}}(\mathbf{u}, p; \mathbf{v}) := b_{\text{vol}}(\mathbf{u}; q) - c(p, q), \quad (13)$$

$$R_{\text{CAV},i}(\mathbf{u}, p_{\text{CAV},i}) := V_{\text{CAV},i}(\mathbf{u}) - V_{\text{CS}}(p_{\text{CAV},i}), \quad (14)$$

where

$$V_{\text{CAV},i}(\mathbf{u}) := \frac{1}{3} \int_{\Gamma_{\text{CAV},i,0}} J(\mathbf{X} + \mathbf{u}) \cdot \mathbf{F}^{-\top} \mathbf{N} \, ds_{\mathbf{X}},$$

with  $\Gamma_{\text{CAV},i,0}$  denoting the closed surface of the  $i^{\text{th}}$  cavity in reference configuration. The expression for cavity volume  $V_{\text{CAV},i}$  follows from applying Nanson's formula to the definition of cavity volume in the current configuration

$$V_{\text{CAV},i} := \frac{1}{3} \int_{\Gamma_{\text{CAV},i}} \mathbf{x} \cdot \mathbf{n} \, ds_{\mathbf{x}}.$$

For a more detailed account on the coupling of nonlinear elastic equations with 0D lumped parameter models we refer to [62].

## 2.2. Consistent Linearization

For the subsequent discretization we need the consistent linearization of (5)–(6) and (9)–(11) and we obtain the following linear saddle-point problem: for each  $(\mathbf{u}^k, p^k) \in V_{\text{gd}} \times Q$ , find  $(\Delta \mathbf{u}, \Delta p) \in V_0 \times Q$  such that

$$a_k(\Delta \mathbf{u}, \Delta \mathbf{v}) + a_{k,\Gamma}(\Delta \mathbf{u}, \Delta \mathbf{v}) + b_k(\Delta p, \Delta \mathbf{v}) = -R_{\text{vol}}(\mathbf{u}^k, p^k; \Delta \mathbf{v}), \quad (15)$$

$$b_k(\Delta q, \Delta \mathbf{u}) - c(\Delta p, \Delta q) = -R_{\text{inc}}(\mathbf{u}^k, p^k; \Delta q), \quad (16)$$

where

$$\begin{aligned} a_k(\Delta \mathbf{u}, \Delta \mathbf{v}) &:= \int_{\Omega_0} \text{Grad } \Delta \mathbf{v} \mathbf{S}_{\text{tot},k} : \text{Grad } \Delta \mathbf{u} \, d\mathbf{X} + \int_{\Omega_0} \boldsymbol{\Sigma}(\mathbf{u}_k, \Delta \mathbf{v}) : \mathbb{C}_{\text{tot},k} : \boldsymbol{\Sigma}(\mathbf{u}_k, \Delta \mathbf{u}) \, d\mathbf{X}, \\ a_{k,\Gamma}(\Delta \mathbf{u}, \Delta \mathbf{v}) &:= p_{\text{ext}} \int_{\Gamma_{N,0}} J_k(\mathbf{F}_k^{-\top} : \text{Grad } \Delta \mathbf{u}) \Delta \mathbf{v} \cdot \mathbf{F}^{-\top} \mathbf{N} \, ds_{\mathbf{X}} \\ &\quad - p_{\text{ext}} \int_{\Gamma_{N,0}} J_k \mathbf{F}_k^{-\top} (\text{Grad } \Delta \mathbf{u})^\top \mathbf{F}_k^{-\top} \mathbf{N} \cdot \Delta \mathbf{v} \, ds_{\mathbf{X}}, \\ b_k(\Delta p, \Delta \mathbf{v}) &:= \int_{\Omega_0} \Delta p \pi(J_k) \mathbf{F}_k^{-\top} : \text{Grad } \Delta \mathbf{v} \, d\mathbf{X}, \end{aligned} \quad (17)$$

using the following abbreviations

$$\begin{aligned} \mathbf{F}_k &:= \mathbf{F}(\mathbf{u}_k), & J_k &:= \det(\mathbf{F}_k), \\ \mathbf{S}_{\text{tot},k} &:= \mathbf{S}_{\text{isc}}|_{\mathbf{u}=\mathbf{u}_k} + p_k \mathbf{S}_{\text{vol}}|_{\mathbf{u}=\mathbf{u}_k}, & \mathbb{C}_{\text{tot},k} &:= \mathbb{C}_{\text{isc}}|_{\mathbf{u}=\mathbf{u}_k} + p_k \mathbb{C}_{\text{vol}}|_{\mathbf{u}=\mathbf{u}_k}, \\ \mathbb{C}_{\text{vol}} &:= k(J) \mathbf{C}^{-1} \otimes \mathbf{C}^{-1} - 2\pi(J) \mathbf{C}^{-1} \odot \mathbf{C}^{-1}, & k(J) &:= J^2 \Theta''(J) + J \Theta'(J), \end{aligned}$$

and  $\mathbb{C}_{\text{isc}}$  given in (C.2). For the deviation of term (17) see Appendix A, other terms in (15)–(16) have been discussed previously, see [63].

In the case of an attached circulatory system we obtain the following linearized system, find  $(\Delta \mathbf{u}, \Delta p, \Delta p_{\text{CAV}})$  such that

$$a_k(\Delta \mathbf{u}, \Delta \mathbf{v}) + a_{k,\Gamma}(\Delta \mathbf{u}, \Delta \mathbf{v}) + b_k(\Delta p, \Delta \mathbf{v}) + l_{\text{surface}}(u^k, \Delta p_{\text{CAV}}; \Delta \mathbf{v}) = -R_{\text{vol}}(\mathbf{u}^k, p^k, p_{\text{CAV}}^k; \Delta \mathbf{v}), \quad (18)$$

$$b_k(\Delta q, \Delta \mathbf{u}) - c(\Delta p, \Delta q) = -R_{\text{inc}}(\mathbf{u}^k, p^k; \Delta q), \quad (19)$$

$$d_k(\Delta \mathbf{u}) - e_k(\Delta p_{\text{CAV}}) = -R_{\text{CAV}}(\mathbf{u}^k, p_{\text{CAV}}^k), \quad (20)$$

where

$$e_k(\Delta p_{\text{CAV}}) := \frac{\partial V_{\text{CAV}}}{\partial p_{\text{CAV}}}, \quad (21)$$

and  $d_k$  defined as in (A.3). The term (21) depends on the chosen model for the circulatory system and a detailed discussion is out of the scope of this work. For a detailed derivation of the explicit representation of the compliance matrix (21) stemming from the model used in Section 3 we refer to [62].

### 2.3. Finite Element Discretization

Here we provide a summary of the finite element discretization used in the subsequent results. The framework builds upon methods previously introduced for isotropic, passive mechanics in [63]. In the following, we extend this approach to anisotropic tissues also allowing for complex EM simulations that are coupled to a 0D system of the circulatory system.

Let  $\mathcal{T}_h$  be a finite element partitioning of  $\bar{\Omega}$  consisting of tetrahedral and/or isoparametric hexahedral finite elements. We assume standard regularity assumptions [54] and invertibility of the isoparametric mapping  $F_K$  from the reference element  $\hat{K}$  to a physical element  $K \in \mathcal{T}_h$ . For tetrahedral elements this poses no additional restrictions, for hexahedral elements we refer to [64] for details. Let further  $\hat{P}_1$  and  $\hat{Q}_1$  denote the space of lowest order linear/trilinear finite element functions on the reference tetrahedron/hexahedron. The discrete analogue to (15)–(16) reads as: given  $(\mathbf{u}_h^k, p_h^k) \in V_{h,\text{gd}} \times Q_h$ , find  $(\Delta \mathbf{u}_h, \Delta p_h) \in V_{h,0} \times Q_h$  such that

$$a_k(\Delta \mathbf{u}_h, \mathbf{v}_h) + a_{k,\Gamma}(\Delta \mathbf{u}_h, \mathbf{v}_h) + b_k(\Delta p_h, \mathbf{v}_h) = -R_{\text{vol}}(\mathbf{u}_h^k, p_h^k; \mathbf{v}_h), \quad (22)$$

$$b_k(q_h, \Delta \mathbf{u}_h) - c(\Delta p_h, q_h) = -R_{\text{inc}}(\mathbf{u}_h^k, p_h^k; q_h) \quad (23)$$

for all  $(\mathbf{v}_h, q_h) \in V_{h,0} \times Q_h$ . The discrete spaces  $V_{h,0}$  and  $Q_h$  are defined as

$$\begin{aligned} V_{h,0} &:= \left\{ \mathbf{v} \in [H_0^1(\Omega_0)]^3 : \mathbf{v}|_K = \hat{\mathbf{v}} \circ F_K^{-1}, \hat{\mathbf{v}} \in [\hat{\mathbb{V}}]^3, \forall K \in \mathcal{T}_h \right\}, \\ Q_h &:= \left\{ q \in L^2(\Omega_0) : q|_K = \hat{q} \circ F_K^{-1}, \hat{q} \in \hat{\mathbb{Q}}, \forall K \in \mathcal{T}_h \right\}, \end{aligned}$$

and additionally we introduce

$$V_{h,\text{gd}} := H_{\text{gd}}^1(\Omega_0) \cap V_{h,0}.$$

#### 2.3.1. Pressure Projection Stabilized Equal Order Pair

The pressure projection stabilization was originally introduced for solving Stokes problems [52] and has also been applied in the context of linear elasticity [65, 66]. Recently, we extended its use to isotropic, nonlinear elasticity [63]. A similar approach can be used for anisotropic materials, we set  $\hat{\mathbb{V}} := \hat{\mathbb{Q}} := \hat{P}_1/\hat{Q}_1$  for tetrahedral or hexahedral elements. To ensure stability, we have to modify the definition of the residuals in (6) and (10) to

$$\begin{aligned} \tilde{R}_{\text{inc}}(\mathbf{u}_h, p_h; q_h) &:= R_{\text{inc}}(\mathbf{u}_h, p_h; q_h) - s_h(p_h, q_h), \\ s_h(p, q) &:= \int_{\Omega_0} \frac{1}{\mu_*} (p - \Pi_h p)(q - \Pi_h q) \, d\mathbf{x}, \end{aligned} \quad (24)$$

where the projection operator  $\Pi_h$  is defined elementwise as

$$\Pi_h q|_K := \frac{1}{|K|} \int_K q \, d\mathbf{x}.$$

In contrast to [63], the parameter  $\mu_*$  is no longer an arbitrary value but set to  $|K|^{1/3}$ ; a choice that showed excellent results for all discussed anisotropic problems in Section 3 as well as isotropic benchmarks in [63]. We note, that the integral in (24) has to be understood as a sum over all the elements of the triangulation of the domain  $\Omega_0$ . For a more comprehensive overview and implementation details we refer to [63].

#### 2.3.2. MINI Element

One of the earliest strategies in constructing a stable finite element pairing for discrete saddle-point problems arising from Stokes Equations is the MINI-Element, dating back to the works of Brezzi et al, see for example [49, 67]. Briefly, the strategy is to enrich the basis of lowest order finite elements by adding a higher degree polynomial with support restricted to the interior of the element. Thus, for the tetrahedral reference element  $\hat{K}$  we define

$$\begin{aligned} \hat{\mathbb{V}} &:= \hat{P}_1 \oplus \{\hat{\psi}_B\} \\ \hat{\mathbb{Q}} &:= \hat{P}_1, \\ \hat{\psi}_B &:= 256\xi_0\xi_1\xi_2(1 - \xi_0 - \xi_1 - \xi_2), \end{aligned}$$

where  $(\xi_0, \xi_1, \xi_2) \in \hat{K}$  see also [68].

For the hexahedral reference element  $\hat{K} = [-1, 1]^3$  we define

$$\begin{aligned}\hat{\mathbb{V}} &:= \hat{Q}_1 \oplus \{\hat{\psi}_{B,1}, \hat{\psi}_{B,2}\} \\ \hat{Q} &:= \hat{Q}_1, \\ \hat{\psi}_{B,1} &:= (1 - \xi_0)^2(1 - \xi_1)^2(1 - \xi_2)^2\hat{\psi}_\alpha, \\ \hat{\psi}_{B,2} &:= (1 - \xi_0)^2(1 - \xi_1)^2(1 - \xi_2)^2\hat{\psi}_\beta,\end{aligned}\tag{25}$$

for  $(\xi_0, \xi_1, \xi_2) \in \hat{K}$  and  $(\alpha, \beta) \in [1, 8]$  denoting the indices of two ansatz functions for diagonal opposite nodes in  $\hat{K}$ , see [63].

Classical results [68] guarantee the stability of the MINI-Element for tetrahedral meshes in the almost incompressible linear elastic case. For hexahedral elements we were able to prove stability in the almost incompressible linear elasticity case provided an enrichment like (25) of the displacement ansatz space by two bubble functions see [63]. Due to the compact support of the bubble functions, static condensation can be applied to remove the interior degrees of freedom during assembly. Static condensation can be done by standard procedures [68] with the exception of follower loads which is discussed in Appendix B. As a result, these degrees of freedom are not needed to be considered in the full global stiffness matrix assembly which is a key advantage of the MINI element.

#### 2.4. Material Models

Arterial and myocardial tissue as modeled in Section 3 is considered as a non-linear, hyperelastic, nearly incompressible, and anisotropic material with a layered organization of fibers. To model this behaviour in our benchmark problems we used strain energy functions of the form (3); namely, the transversely isotropic constitutive law by Guccione et al. [69]

$$\Psi(\mathbf{C}) = U(J) + \bar{\Psi}(\bar{\mathbf{C}}) \quad \text{with} \quad \bar{\Psi}(\bar{\mathbf{C}}) = \frac{a}{2} [\exp \mathcal{Q}(\bar{\mathbf{C}}, \mathbf{a}_i) - 1]\tag{26}$$

with  $a > 0$  kPa a scaling parameter,  $\mathbf{a}_i$  fiber directions, and  $\mathcal{Q}$  a function in terms of scalar strain components. Further, we compared the standard formulation of a separated Fung-type exponential model

$$\Psi(\mathbf{C}) = U(J) + \bar{\Psi}_{AS}(\bar{\mathbf{C}}) \quad \text{with} \quad \bar{\Psi}_{AS}(\bar{\mathbf{C}}) = \bar{\Psi}_{iso}(\bar{\mathbf{C}}) + \bar{\Psi}_{aniso}(\bar{\mathbf{C}}, \mathbf{a}_i)\tag{27}$$

with the formulation using an unsplit deformation gradient for the anisotropic contribution

$$\Psi(\mathbf{C}) = U(J) + \Psi_{WAS}(\mathbf{C}) \quad \text{with} \quad \Psi_{WAS}(\mathbf{C}) = \bar{\Psi}_{iso}(\bar{\mathbf{C}}) + \Psi_{aniso}(\mathbf{C}, \mathbf{a}_i),\tag{28}$$

introduced in [70, 71]. The specific form of the volumetric,  $U(J)$ , isotropic,  $\bar{\Psi}_{iso}$ , and anisotropic,  $\bar{\Psi}_{aniso}/\Psi_{aniso}$ , contributions will be discussed later for each of the benchmark problems.

### 3. Numerical Examples

Biomechanical applications often require highly resolved meshes and thus efficient and massively parallel solution algorithms for the linearized system of equations become an important factor to deal with the resulting computational load. Extending our previous implementations for cardiac EM [72] we used the software *Cardiac Arrhythmia Research Package* (CARP) [73] which makes use of the MPI based library *PETSc* [74]. We solve the stabilized saddle-point problem (22)–(23) by using a GMRES method with a block preconditioner based on a smoothed aggregation algebraic multigrid (GAMG) approach which is incorporated in *PETSc* [75].

In all of the following benchmark problems our goal was to study the performance and accuracy of different finite element discretizations, namely i) *Q1/P1-P0-AS*: discretization with piecewise linear displacements and piecewise constant pressure using the strain energy function (27); ii) *Q1/P1-P0-WAS*: discretization with piecewise linear displacement and piecewise constant pressure using the strain energy function (28); iii) *Projection*: equal order discretization with piecewise linear displacements and pressure, stabilized as described in Section 2.3.1 using the strain energy function (27); iv) *MINI*: discretization using MINI elements as described in Section 2.3.2 using the strain energy function (27).

### 3.1. Extension, Inflation and Torsion of a Simplified Artery Model

*Simulation setup.* First, we show the applicability of our proposed methods to a benchmark problem from Gültekin et al. [76] where a simplified artery model is represented by a thick-walled cylindrical tube. The dimensions of this idealized geometry with its centerline on the  $z$ -axis are as follows: height  $H = 10$  mm, inner radius  $R_1 = 8$  mm, and outer radius  $R_2 = 10$  mm. Two symmetric families of fibers,  $\mathbf{f}_0$  and  $\mathbf{s}_0$  are immersed in the tissue, having an angle of  $40^\circ$  with circumferential  $\theta$ -axis, see Figure 1A. As for loading, a

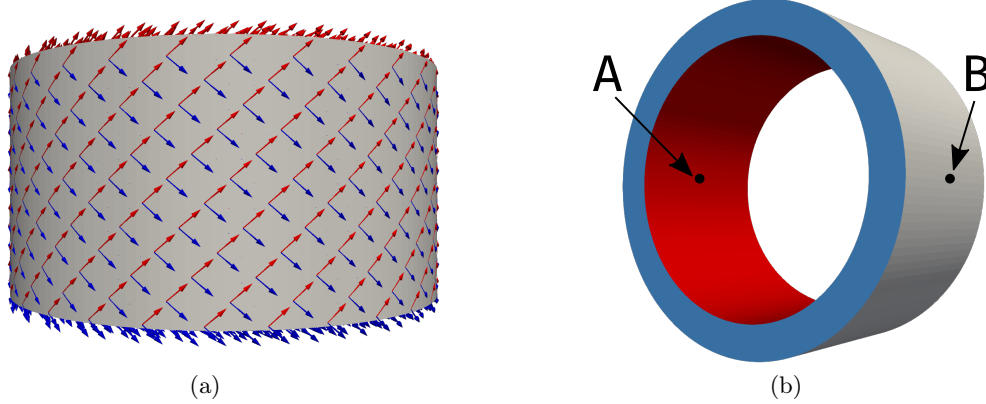


Figure 1: *Artery benchmark*: Geometry, fiber distribution, and boundary conditions. Figure (a) shows the fiber arrangement and Figure (b) shows the geometry and color-coded boundaries for the application of the boundary conditions and the evaluation points A, and B for mesh convergence.

monotonically increasing displacement up to 2 mm superimposed by a monotonically increasing torsion up to  $60^\circ$  is applied on the top of the tube (marked blue in Figure 1B). Additionally, a linearly increasing pressure (follower load) up to 500 mmHg is applied on the inside of the tube (marked red in Figure 1B). Finally, the lower part of the tube is clamped at zero displacement.

The material is described by the strain-energy function (27),  $\bar{\Psi}_{AS}$ , with

$$\Theta(J) := J - 1, \quad \bar{\Psi}_{iso}(\bar{\mathbf{C}}) := \frac{\mu}{2} (\bar{I}_1 - 3),$$

$$\bar{\Psi}_{aniso}(\bar{\mathbf{C}}, \mathbf{f}_0, \mathbf{s}_0) := \frac{k_1}{2k_2} \sum_{i=4,6} \left( \exp \left( k_2 (\bar{I}_i - 1)^2 \right) - 1 \right),$$

and invariants

$$\bar{I}_1 := \text{tr}(\bar{\mathbf{C}}), \quad \bar{I}_4 := \bar{\mathbf{C}} : \mathbf{f}_0 \otimes \mathbf{f}_0, \quad \bar{I}_6 := \bar{\mathbf{C}} : \mathbf{s}_0 \otimes \mathbf{s}_0,$$

and analogously with  $\Psi_{aniso}(\mathbf{C}, \mathbf{f}_0, \mathbf{s}_0)$  for the WAS formulation,  $\Psi_{WAS}$ , (28). Material parameters were taken from [76, Table 1], i.e.,  $\kappa = 5000$  kPa,  $\mu = 10$  kPa,  $k_1 = 500$  kPa, and  $k_2 = 2.0$ . In case of the stabilized equal-order elements (Projection and MINI), we set  $1/\kappa = 0$  to render the material incompressible. To assess mesh convergence simulations were performed on seven discretization levels, see Table 1.

*Results.* A comparison of the radial,  $\sigma_{rr}$ , the circumferential,  $\sigma_{\theta\theta}$ , and the axial,  $\sigma_{zz}$ , components of the Cauchy stress tensor is shown in Figure 2 for the finest discretization level  $\ell = 7$ . We see that with the exception of the lowest order discretizations with anisotropic splitting (Q1/P1-P0-AS) the stress distribution is very similar and also matches results in Gültekin et al. [76]. The observation that simulations with Q1/P1-P0-AS are not accurate for this benchmark problem is further emphasized in Figures 3 and 4. Here, Figure 3 shows the displacements ( $u_x, u_y, u_z$ ) and Figure 4 shows the stress components ( $\sigma_{rr}, \sigma_{\theta\theta}, \sigma_{zz}$ ) at the evaluation points A and B over the discretization levels. In agreement with [76] the lowest order discretization with anisotropic splitting converges to a lower value than the other discretization types hinting at possible locking phenomena. All other formulations perform similarly well. Here, discrepancies at the finest level  $\ell = 7$  are rather due to differences in the meshes for tetrahedral and hexahedral grids.

Figure 5 shows a distribution of the Jacobian  $\det(\mathbf{F})$  on the finest level  $\ell = 7$ . Unsurprisingly, with a mean value  $\mu$  close to 1 the saddle-point formulations (Projection, MINI) satisfy incompressibility better

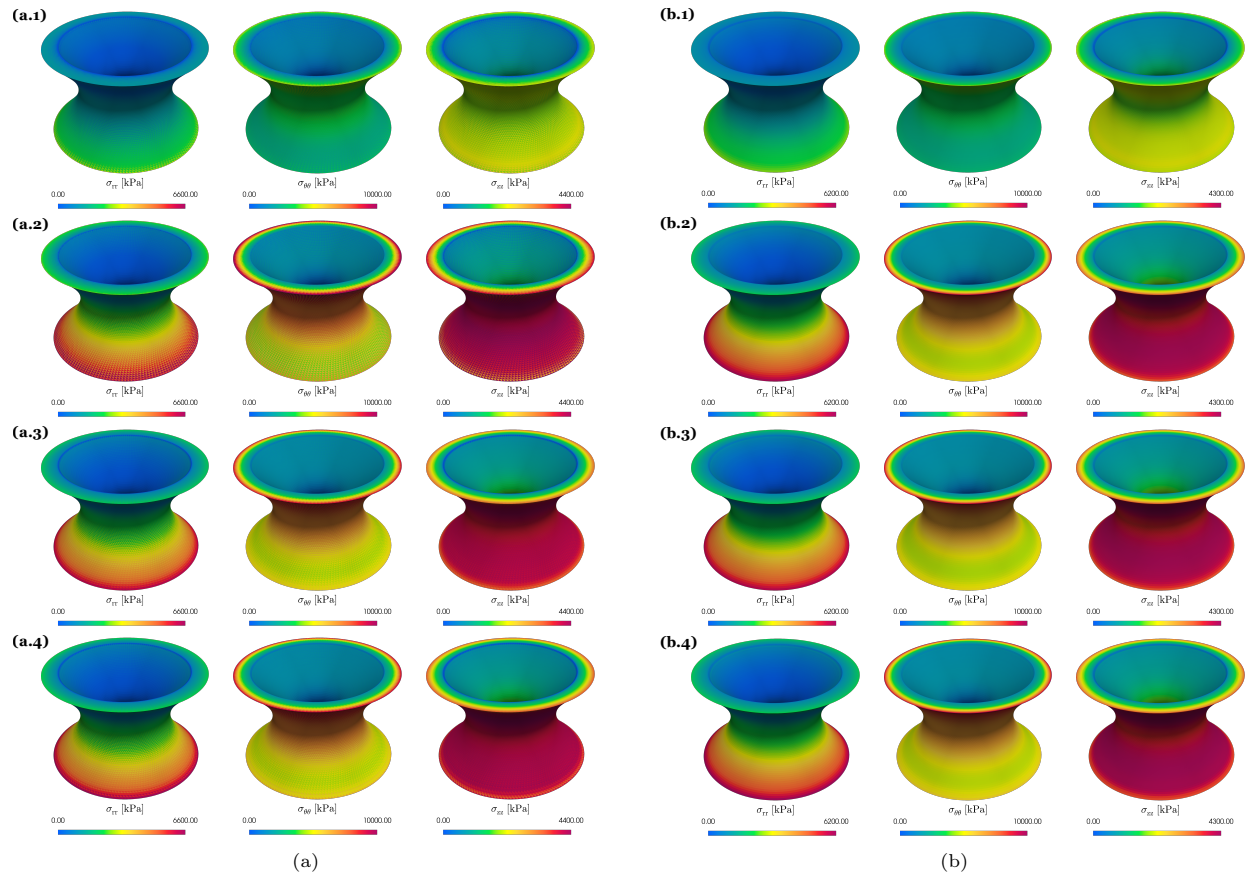
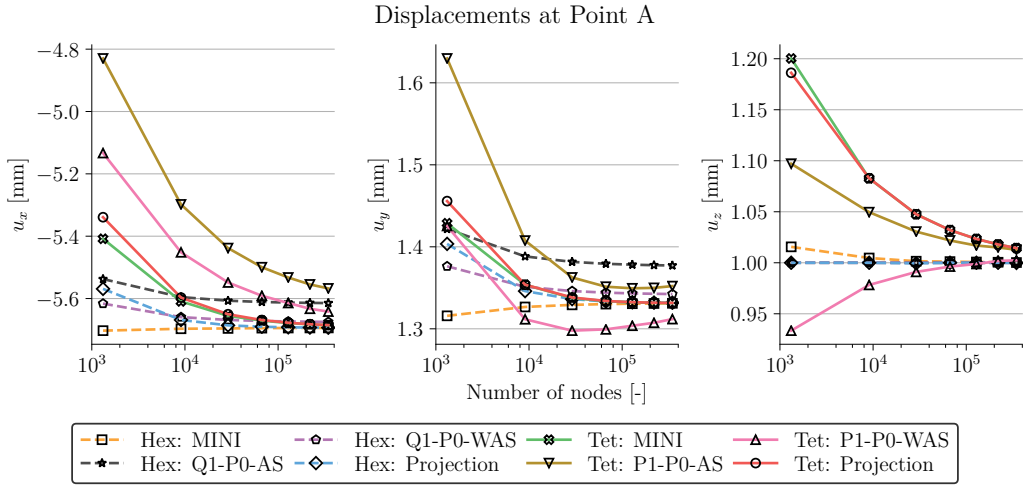
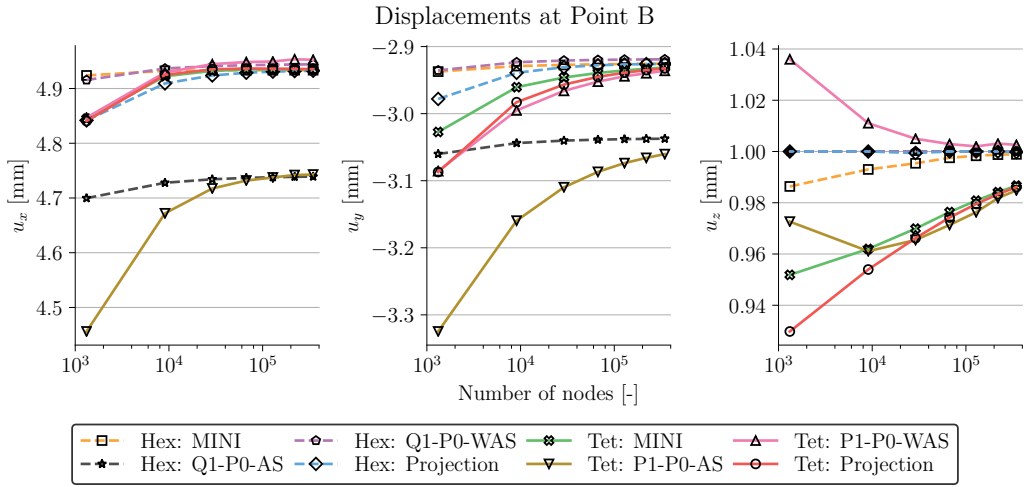


Figure 2: *Artery benchmark*: Stress distribution for (a) tetrahedral and (b) hexahedral elements. Shown are the radial,  $\sigma_{rr}$ , circumferential,  $\sigma_{\theta\theta}$ , and longitudinal stresses,  $\sigma_{zz}$ , on the finest discretization level  $\ell = 7$ . The rows 1, 2, 3, 4 correspond to Q1-P0-AS, Q1-P0-WAS, Projection, and MINI, respectively.

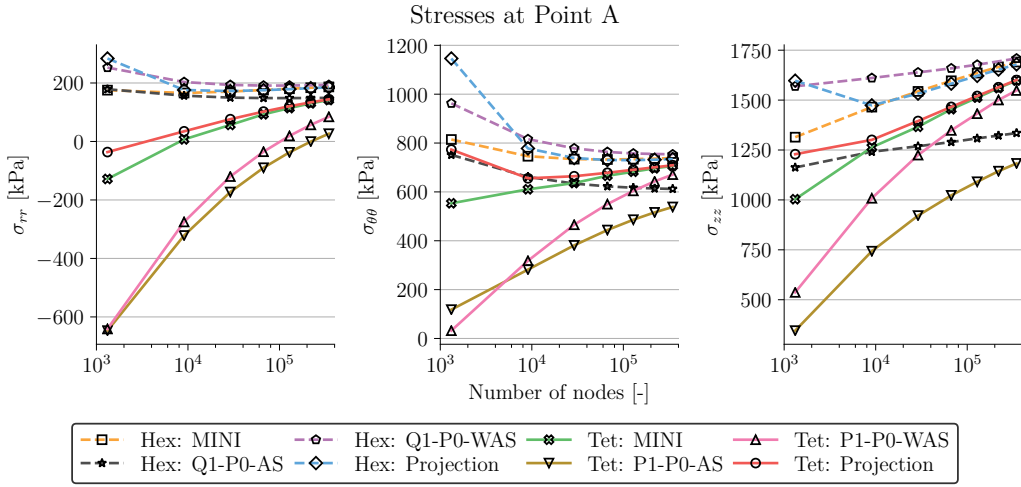


(a)

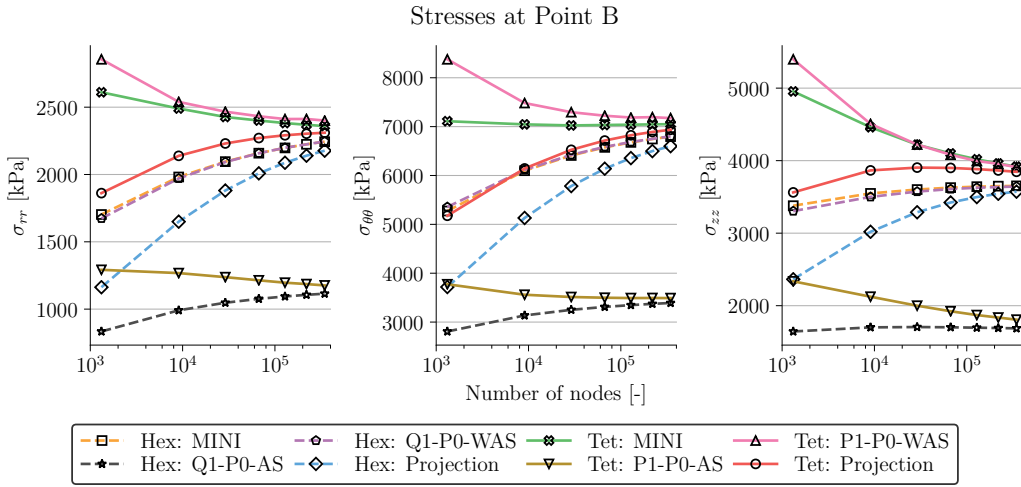


(b)

Figure 3: *Artery benchmark*: Mesh convergence. Shown are the individual displacement values at (a) Point A and (b) Point B for increasing mesh resolution and finite elements.

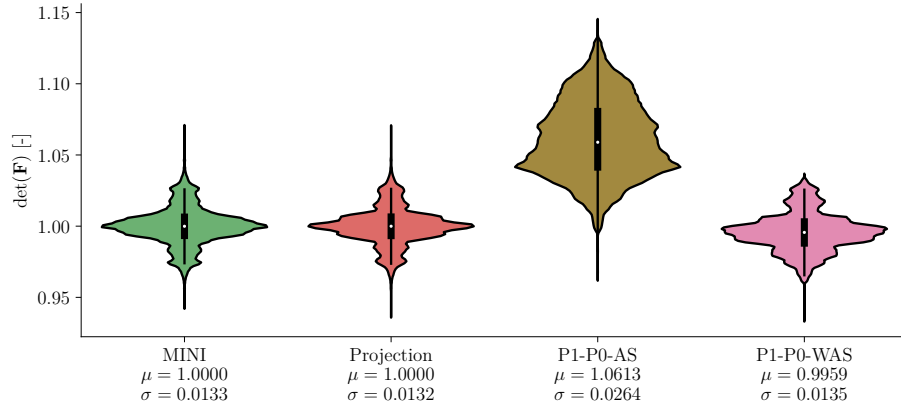


(a)

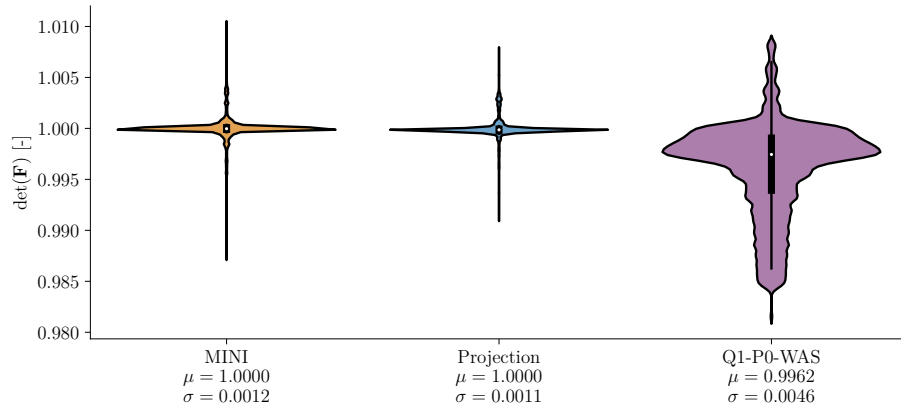


(b)

Figure 4: *Artery benchmark*: Mesh convergence. Shown are the individual stresses at (a) Point A and (b) Point B for increasing mesh resolution and finite elements.



(a)



(b)

Figure 5: *Artery benchmark*: Jacobian distribution for (a) tetrahedral and (b) hexahedral elements. Shown are violin plots of the Jacobian distribution  $\det(\mathbf{F})$  on the finest discretization level at maximum loading for the various finite elements. Additionally, the mean  $\mu$  and standard deviation  $\sigma$  is given. Q1-P0-AS has been excluded from plot (b) as values were significantly higher compared to other element types.

than the penalty formulations (P1/Q1-P0-AS, P1/Q1-P0-WAS). While the AS formulation led to a small increase in volume ( $\mu > 1$ ), the WAS formulation resulted in a slightly reduced volume ( $\mu < 1$ ).

*Numerical performance.* Computational times for the simulation using different element types are given in Figure 6; left, for the coarse problem ( $\ell = 1$ ) and right, for the finest grid ( $\ell = 7$ ). For all cases we used a relative error reduction of  $\epsilon = 10^{-8}$  for the GMRES linear solver and a relative error reduction of  $\epsilon = 10^{-6}$  for the residual of the Newton method. Using a load stepping scheme, this required a total number of 100 linear solving steps for the coarse problem and 1000 linear solving steps for the fine problem to arrive at the final prescribed displacement and inner pressure of 500 mmHg.

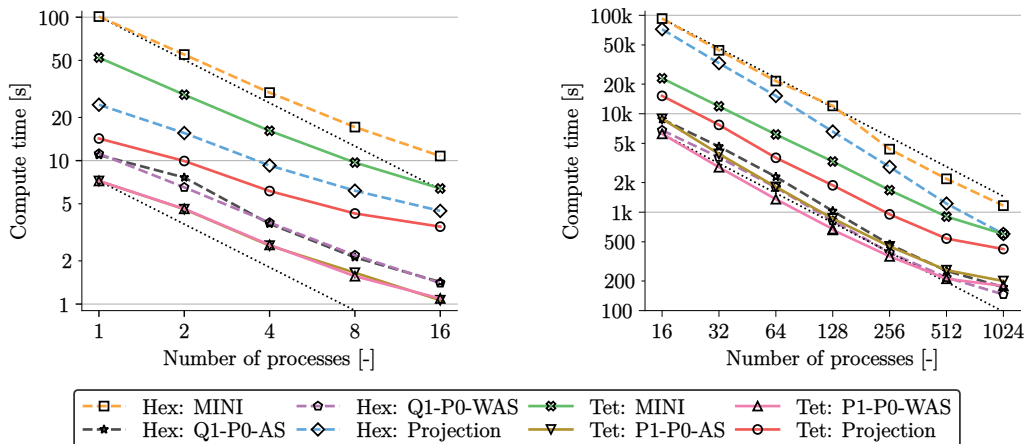


Figure 6: *Artery benchmark*: Strong scaling results for the different element types for the coarsest grid ( $\ell = 1$ , left) and the finest grid ( $\ell = 7$ , right). Simulations were performed on 1 to 16 cores of a standard desktop computer for the coarse problem and on 16 to 1024 cores on Archer2.

Strong scaling was achieved for the coarse problem up to 16 cores on a desktop machine (AMD Ryzen Threadripper 2990X), see Figure 6, left. Here, computational times were averaged over 5 runs using the same setup and range from 1s to 1.5s for penalty formulations (P1/Q1-P0-AS, P1/Q1-P0-WAS). For the projection-stabilized element compute times were around 3 times slower (Tet Projection: 3.5s, Hex Projection: 4.5s) while for the MINI element compute times were around 7 times slower (Tet MINI: 6.4s, Hex MINI: 10.8s).

For the fine grid strong scaling was obtained up to 1024 cores on Archer2 (<https://www.archer2.ac.uk/>), see Figure 6, right. Computational times using 1024 cores were between 146s and 200s for penalty formulations (P1/Q1-P0-AS, P1/Q1-P0-WAS); around 3 times slower for the projection-stabilized elements (Tet Projection: 422s, Hex Projection: 601s); and around 6 times slower for MINI elements (Tet MINI: 600s, Hex MINI: 1166s).

Table 1: *Artery benchmark*: properties of idealized artery meshes used in Section 3.1.

$\ell$	Elements (Hex)	Elements (Tet)	Nodes
1	960	5760	1320
2	7680	46 080	9072
3	25 920	155 520	29 016
4	61 440	368 640	66 912
5	120 000	720 000	128 520
6	207 360	1 244 160	219 600
7	329 280	1 975 690	345 912

*Discussion.* In accordance with Gültekin et al. [76] we have shown for this benchmark that the concept Q1/P1-P0-WAS is able to match quasi-incompressible responses compared to the gold standard of locking-free elements. For this extreme loading case standard Q1/P1-P0 elements cannot reproduce accurate stress distributions; not even on very fine grids, see Figure 4(b).

Further, this benchmark highlights the high efficiency of our methods. While the authors in [76] reported computational times on one 3.2GHz CPU unit that were 1 minute for Q1-P0-WAS elements and 20 minutes for their gold-standard (Q1-P0 elements using an Augmented Lagrangian method) we have achieved compute times on a comparable 3.0GHz CPU unit and the same mesh that were 11 seconds for Q1-P0-WAS elements and 24 seconds for locking-free Hex Projection elements, see Figure 6, left. That means that stabilization techniques presented in this paper allow up to 50 times faster execution times for this benchmark compared to other gold standard methods.

Due to a higher number of linear iterations and higher matrix assembly times, simulations with hexahedral meshes were more expensive compared to simulations with tetrahedral grids. However, as also observed, e.g., by Chamberland et al. [77] hexahedral elements were slightly more accurate than their tetrahedral equivalent.

### 3.2. Inflation and Active Contraction of a Simplified Ventricle

*Simulation setup.* To verify our EM setup we repeated the inflation and active contraction benchmark from Land et al. [78]. We generated the reference geometry of an idealized ventricle as a tetrahedral mesh of a truncated ellipsoid and prescribed a local orthonormal coordinate system with fiber,  $\mathbf{f}_0$ , sheet,  $\mathbf{s}_0$ , and sheet-normal,  $\mathbf{n}_0$ , directions according to this paper. We constructed three levels of refinement, see Table 2 for discretization details.

Table 2: *Ellipsoid benchmark:* properties of idealized ventricle meshes used in Section 3.2.

$\ell$	Elements	Nodes
1	20 709	4732
2	201 495	38 896
3	1 747 845	312 784

As material we used the transversely isotropic law by Guccione et al. [69], see Equation (26), with  $\Theta(J) := \ln(J)$  and

$$\mathcal{Q} := b_f(\mathbf{f}_0 \cdot \bar{\mathbf{E}}\mathbf{f}_0)^2 + b_t[(\mathbf{s}_0 \cdot \bar{\mathbf{E}}\mathbf{s}_0)^2 + (\mathbf{n}_0 \cdot \bar{\mathbf{E}}\mathbf{n}_0)^2 + 2(\mathbf{s}_0 \cdot \bar{\mathbf{E}}\mathbf{n}_0)^2] + 2b_{fs}[(\mathbf{f}_0 \cdot \bar{\mathbf{E}}\mathbf{s}_0)^2 + (\mathbf{f}_0 \cdot \bar{\mathbf{E}}\mathbf{n}_0)^2].$$

Constitutive parameters were  $a = 2$  kPa,  $b_f = 8$ ,  $b_t = 2$ , and  $b_{fs} = 4$ . In the benchmark paper the material is considered to be fully incompressible, hence, we chose  $1/\kappa = 0$  for the saddle-point formulation (Projection, MINI). For the penalty formulation (P1-P0 elements) we chose  $\kappa = 1000$  kPa which was the best trade-off between convergence of the solver for all three levels in Table 2, near incompressibility, and minimization of locking effects.

As the material law above does not allow for a WAS formulation we repeated the benchmark using a separated Fung-type exponential model as in Equation (27). In particular, we chose a Holzapfel–Ogden material [79] of the form

$$\begin{aligned} \Theta(J) &:= \ln(J), & \bar{\Psi}_{\text{iso}}(\bar{\mathbf{C}}) &:= \frac{a}{2b} \{ \exp[b(\bar{I}_1 - 3)] - 1 \} \\ \bar{\Psi}_{\text{aniso}}(\bar{\mathbf{C}}, \mathbf{f}_0, \mathbf{s}_0, \mathbf{n}_0) &:= \sum_{i=f,n} \frac{a_i}{2b_i} \{ \exp[b_i(\bar{I}_{4i} - 1)^2] - 1 \} + \frac{a_{fs}}{2b_{fs}} \{ \exp[b_{fs}(\bar{I}_{8fs})^2] - 1 \}, \end{aligned} \quad (29)$$

with invariants

$$\bar{I}_1 := \text{tr}(\bar{\mathbf{C}}), \quad \bar{I}_{4f} = \max(\mathbf{f}_0 \cdot \bar{\mathbf{C}}\mathbf{f}_0, 1), \quad \bar{I}_{4n} = \max(\mathbf{n}_0 \cdot \bar{\mathbf{C}}\mathbf{n}_0, 1),$$

such that contributions of compressed fibers are excluded, and the interaction-invariant

$$\bar{I}_{8fs} = \mathbf{f}_0 \cdot \bar{\mathbf{C}}\mathbf{s}_0.$$

Analogously, we used the constitutive equation above with  $\Psi_{\text{aniso}}(\mathbf{C}, \mathbf{f}_0, \mathbf{s}_0, \mathbf{n}_0)$  for the WAS formulation. Material parameters were taken from [80],  $a = 0.809$  kPa,  $b = 7.474$ ,  $a_f = 1.911$  kPa,  $b_f = 22.063$ ,  $a_n = 0.227$  kPa,  $b_n = 34.802$ ,  $a_{fs} = 0.547$  kPa, and  $b_{fs} = 5.691$ , fitted to human myocardial experiments in [81].

*Results.* For the transversely isotropic law (26), we compared our results to selected reference solutions from the benchmark paper [78], namely, the result from IBM with the Cardioid framework [82] using P2-P1 elements and the result from Simula with FEniCS [83] using two-dimensional P2-P1 elements. First, the final location of the apex is measured and, second, circumferential, longitudinal, and radial strains at the endocardium, epicardium, and midwall are calculated on points along apex-to-base lines, see [78] for more details. Results show that the apex location Figure 7(a) and strains Figure 8 are very similar for the finest level ( $\ell = 3$ ) for all chosen element types. For the level  $\ell = 2$  the strain solution using simple P1-P0 elements is not converged showing differences to the benchmark solutions especially in boundary regions at the apex (p1) and the base (p10), see Figure 8(a).

We repeated simulations as above measuring the final apex location and calculating strains along apex-to-base lines using the orthotropic law (29). We compared results using P1-P0-WAS, P1-P0-AS, projection-stabilized, and MINI elements in Figure 7(b) and Figure 9. Apex locations are very similar for all element types, however, strains are different, especially in boundary regions close to the apex and the base. We can see in Figure 9 that even for the finest level ( $\ell = 3$ ) the strain solution for both P1-P0 formulations is not converged while solutions for stabilized elements are already very similar for levels  $\ell = 2$  and  $\ell = 3$ .

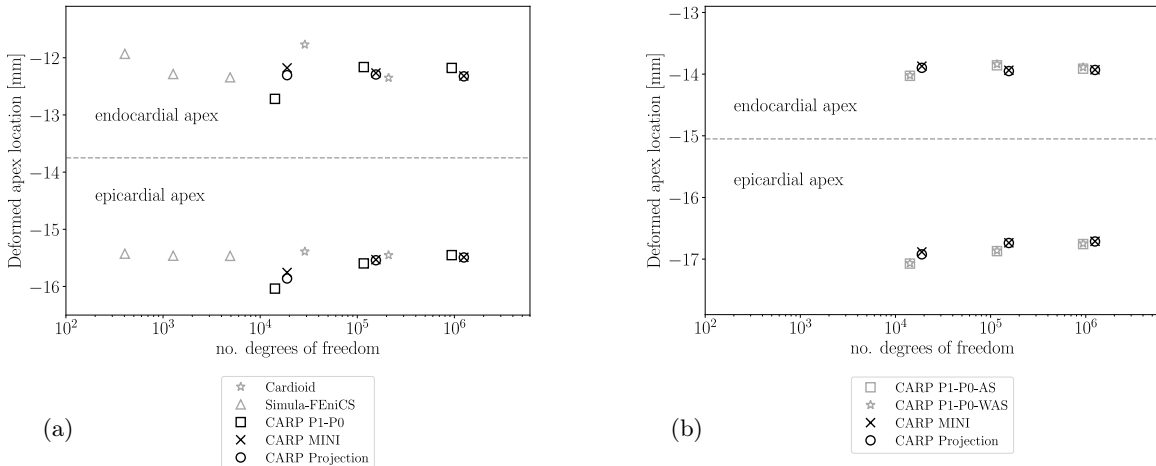


Figure 7: *Ellipsoid benchmark:* apex location. The dashed line separates results for the deformed positions of the apex at the endo- and epicardium. (a) Guccione material with comparison to benchmark results (in gray) presented in [78]; (b) Holzapfel–Ogden material with comparison to P1-P0-WAS formulation.

*Discussion.* For the transversely-isotropic Guccione material model strains with the presented projection-stabilized and MINI elements match results using higher order P2-P1 elements even on coarser grids. Here, also linear tetrahedral elements seem to be accurate given a fine enough discretization; this behavior was also observed in [78].

In contrast to that, for the orthotropic Holzapfel–Ogden material, we see in Figure 9 that P1-P0 elements cannot always accurately reproduce strains even on the finest grid. On the other hand we can assume that strains are accurate and almost converged for projection-stabilized and MINI elements as results for levels 2 and 3 are very similar. Interestingly, for this benchmark, we see no difference in accuracy between the standard P1-P0 and the P1-P0-WAS formulation. Most likely the reason for this is that parameters fitted to human myocardial data [80] are not as stiff in fiber direction compared to the more extreme artificial benchmark case in Section 3.1. Overall, both approaches with simple linear elements fail to match results from gold-standard elements, especially in boundary regions.

### 3.3. 3D-0D closed-loop model of the heart and circulation

*Simulation setup.* Finally, we show the applicability of our method to an advanced model of computational cardiac EM. Here, a 3D model of bi-ventricular EM is coupled to the physiologically comprehensive 0D CircAdapt model representing atrial mechanics and closed-loop circulation. In the present paper, the myocardium of the ventricles was modeled as a nonlinear hyperelastic, (nearly) incompressible and orthotropic

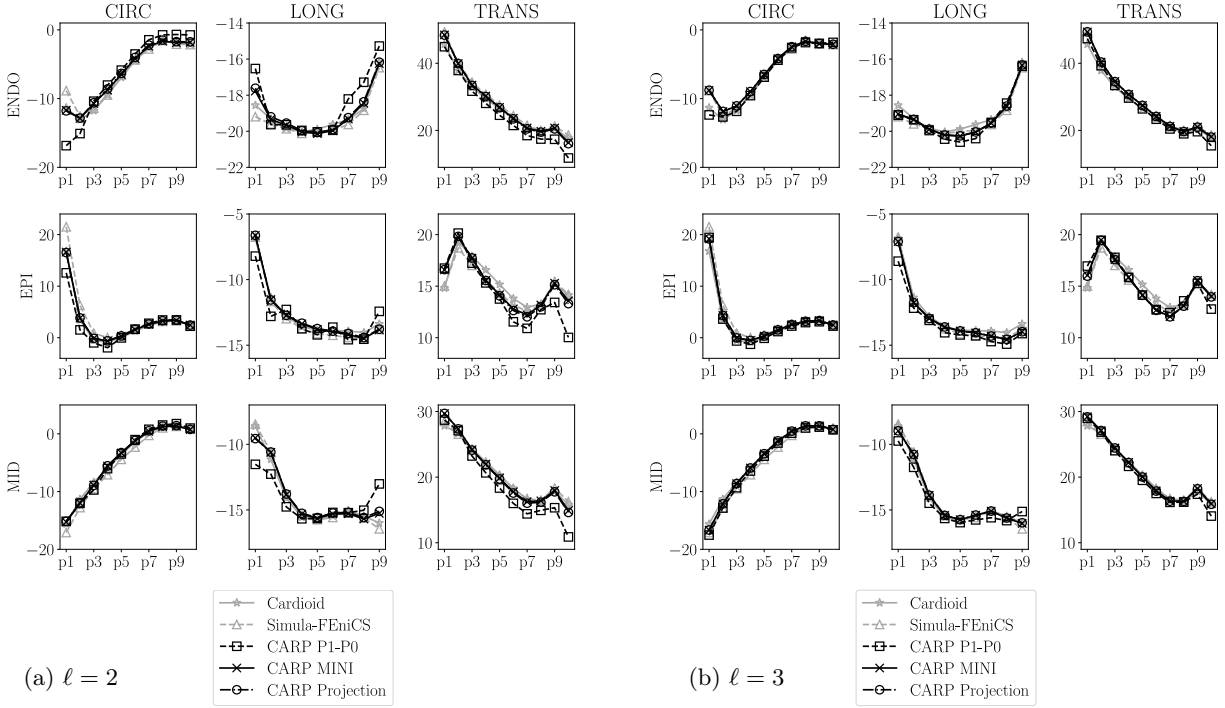


Figure 8: *Ellipsoid benchmark, Guccione material*: longitudinal (LONG), circumferential (CIRC), and radial (TRANS) strains at endocardium, epicardium, and midwall. Index of points increases from the apex to the base. Own results (in black) are compared to benchmark results (in gray) presented in [78].

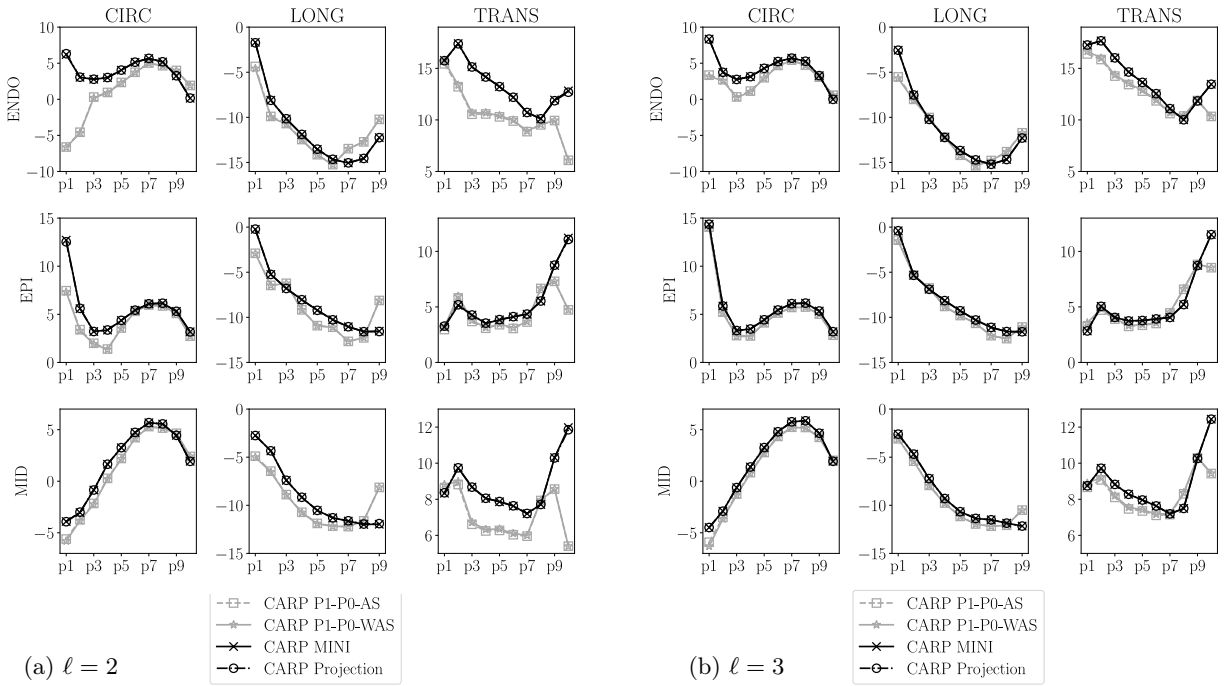


Figure 9: *Ellipsoid benchmark, Holzapfel-Ogden material*: longitudinal (LONG), circumferential (CIRC), and radial (TRANS) strains at endocardium, epicardium, and midwall. Index of points increases from the apex to the base. P1-P0 elements (in gray) are compared to stabilized elements (in black).

material as in Equation (27). In particular, for this application, we chose the model proposed by Gültekin et al. [84]

$$\Theta(J) := \ln(J), \quad \bar{\Psi}_{\text{iso}}(\bar{\mathbf{C}}) := \frac{a}{2b} \{ \exp [b(\bar{I}_1 - 3)] - 1 \}$$

$$\bar{\Psi}_{\text{aniso}}(\bar{\mathbf{C}}, \mathbf{f}_0, \mathbf{s}_0) := \sum_{i=f,s} \frac{a_i}{2b_i} \{ \exp [b_i(\bar{I}_{4i} - 1)^2] - 1 \} + \frac{a_{fs}}{2b_{fs}} \{ \exp [b_{fs}(\bar{I}_{8fs})^2] - 1 \},$$

with modified unimodular fourth-invariants to support dispersion of fibers

$$I_{4i}^* = \kappa_i \bar{I}_1 + (1 - 3\kappa_i) I_{4i}, \quad i \in f, s$$

and standard invariants

$$\bar{I}_1 := \text{tr}(\bar{\mathbf{C}}), \quad \bar{I}_{8fs} = \mathbf{f}_0 \cdot \bar{\mathbf{C}} \mathbf{s}_0.$$

Analogously, we used the constitutive equation above with  $\Psi_{\text{aniso}}(\mathbf{C}, \mathbf{f}_0, \mathbf{s}_0)$  for the WAS formulation.

A reaction-eikonal model [85] was used to generate electrical activation sequences. Cellular dynamics were described by the Grandi–Pasqualini–Bers model [86] coupled to the Land–Niederer model [87] to account for length and velocity dependence of active stress generation, see also Augustin et al. [72] for more details on this strong coupling as well as Regazzoni and Quarteroni [88] for implementation details on the velocity-dependent active stress model. The active stress tensor is computed according to [89] as

$$\mathbf{S}_a = S_a \left( \frac{\kappa_f}{1 - 2\kappa_f} \mathbf{C}^{-1} + \frac{1 - 3\kappa_f}{1 - 2\kappa_f} (\mathbf{f}_0 \cdot \mathbf{C} \mathbf{f}_0)^{-1} \mathbf{f}_0 \otimes \mathbf{f}_0 \right),$$

where  $S_a$  is the scalar valued active stress generated in the cardiac myocytes and  $\kappa_f$  is the same dispersion parameter as above.

For the time integration of Cauchy’s equation of motion we used a variant of the generalized- $\alpha$  integrator [90] with spectral radius  $\rho_\infty = 0$  and damping parameters  $\beta_{\text{mass}} = 0.1 \text{ ms}^{-1}$ ,  $\beta_{\text{stiff}} = 0.1 \text{ ms}$ .

*Bi-ventricular finite element models.* The bi-ventricular geometry was created according to [62] with an average spatial resolution of 1.3 mm for the LV and 1.2 mm for the RV. The resulting mesh used for simulations consisted of 557 316 elements and 111 234 nodes. Fiber and sheet directions were computed by a rule-based method [91] with fiber angles changing linearly from  $-60^\circ$  at the epicardium to  $+60^\circ$  at the endocardium [92].

*Boundary conditions.* Boundary conditions on the epicardium were modeled using spatially varying normal Robin boundary conditions [93] to simulate *in-vivo* constrains imposed by the pericardium. The basal cut plane was constrained by omni-directional spring type boundary conditions. The 3D ventricular PDE model was coupled to the 0D ODE model *CircAdapt* [94] representing cardiovascular system dynamics according to Augustin et al. [62]. An *ex-vivo* setting without pericardial boundary conditions is used to calibrate parameters replicating *ex-vivo* passive inflation experiments by Klotz et al. [95].

*Parameterization.* Passive material parameters  $a = 0.4$ ,  $b = 6.55$ ,  $a_f = 3.05$ ,  $b_f = 29.05$ ,  $a_s = 1.25$ ,  $b_s = 36.65$ ,  $a_{fs} = 0.15$ , and  $b_{fs} = 6.28$  were taken from [84]. Dispersion parameters have been identified previously by mechanical experiments on passive cardiac tissue by Sommer et al. [81] and are set to  $\kappa_f = 0.08$  and  $\kappa_s = 0.09$ .

To eliminate potential differences in stress/strain due to parameterization we fitted parameters to achieve similar pressure-volume (PV) loops and a similar end-diastolic PV relationship (EDPVR) for all element types. First, initial passive material parameters above were fitted to the empiric description of the EDPVR by Klotz et al. [95]. For each element type we used a backward displacement algorithm and boundary conditions replicating experiments in [95] according to Marx et al. [96], see Figure 10. This fitting resulted in multiplicative scaling factors of 0.4529 (P1-P0 elements) and 0.9582 (locking-free elements) for the stress-like material parameters ( $a$ ,  $a_f$ ,  $a_s$ ,  $a_{fs}$ ); and in multiplicative scaling factors of 1.0322 (P1-P0 elements) and 0.7981 (locking-free elements) for the dimensionless parameters ( $b$ ,  $b_f$ ,  $b_s$ ,  $b_{fs}$ ). The list of fitted passive parameters is given in Table 3.

Active stress parameters were fitted using locking-free elements to reach a target peak pressure of 105 mmHg in the LV. Using the same active stress parameters, the simulations with P1-P0 elements resulted in slightly higher peak pressure, 109.2 mmHg, see Figure 11 (a). The end-diastolic state remained

almost unchanged while the ejection fraction increased slightly. We attribute this to a higher contractility of the elements when the tissue is not modeled as a fully incompressible continuum. To achieve similar PV loops for P1-P0 elements, simulations were repeated with reduced active tension  $T_{\text{ref}}^\bullet$ . See Table 3 for a summary of all active stress parameters. Simulations parameters of the circulatory system were set as in Augustin et al. [62] with a cycle length of 0.585 s.

*Results.* First, simulation results in Figure 10 (a) show that the passive parameterization - that was performed individually for all element types - allowed to reach the predicted stress-free volume and the given end-diastolic volume almost perfectly while reproducing the shape of the Klotz EDPVR curve. Boundary conditions for this experiment correspond to the *ex-vivo* setting described above replicating passive inflation experiments [95]. With fitted material parameters we repeat the backward displacement algorithm to get a stress-free reference geometry with *in-vivo* boundary conditions to model the constraints imposed by the pericardium. Loading the found stress-free configuration to end-diastolic pressure results in loading curves as shown in Figure 10 (b). These loading curves are almost identical for all element types. The pre-stressed configuration after this initial loading phase matches the geometry obtained from imaging and serves as the starting point for EM heart beat experiments as described in the following.

To get to a converged solution of the closed-loop 3D-0D system we simulated 30 heart beats for each finite element setting: 18 init beats with 1 Newton step corresponding to a semi-implicit (linearly-implicit) discretization method [97]; 10 beats with 2 Newton steps which is required to get a correct update due to the velocity dependence of the active-stress model; and two final beats with a fully converged Newton with a relative error reduction of the residual of  $\epsilon = 10^{-6}$ .

See Figure 11 (a) for a comparison of the final three pressure-volume loops with the same active stress parameters which resulted in higher pressures for P1-P0 elements. In Figure 11 (b)–(d) we show traces for the refitted active stress parameters as described above. Here, the final three P-V loops in Figure 11 (b) coincide. Hence, the solution is converged and there is also no difference between the simulation with two Newton steps and the fully converged Newton method. This also holds for true for pressures in the ventricles and adjacent arteries, see Figure 11 (c), in- and outflow traces Figure 11 (d), and strains/stresses.

Looking at myocardial mass in Figure 10 (c) we can see that for projection-stabilized and MINI elements the mass stays at the initial value of  $133.56 \text{ cm}^3$  all the time during the final three beats; this is expected as the tissue is modeled to be fully incompressible ( $1/\kappa = 0$ ). For P1-P0 elements using a penalty formulation ( $\kappa = 650 \text{ kPa}$ ) the tissue is nearly incompressible and especially during the ejection phase the myocardial mass decreases slightly: maximal 1.17% for P1-P0-AS and 1.38% for P1-P0-WAS elements.

In contrast to pressure, volume, and flow traces, stresses show a very different pattern when comparing locking-free to simple P1-P0 elements, see Figure 12. In this plot we show element-wise, total first principal stress at three time points marked by A, B, and C in the P-V loop in Figure 11 (b) which represent A, the most expanded (end-diastole), B, the highest total stress (peak systole), and C, the most contracted (beginning of filling phase) states of the ventricles. Especially at end-diastole Figure 12 (a) and the beginning of the filling phase Figure 12 (c) where passive stress dominates and active stress is close to zero we see a distinct checkerboard pattern for P1-P0 elements while solutions for projection-stabilized and MINI elements are smooth. Also in violin plots showing the stress distribution over the whole tissue domain we see a clear difference for these time points, see Figure 13 (a) and (c). On the other hand, the stress distribution is very similar for all element types at peak-systole where active stress dominates, see Figure 12 (b) and Figure 13 (b).

*Numerical performance.* Computational times for the simulation using different element types are given in Table 4. Simulations were performed on 128 cores of Archer2 and we distinguish between solver-time,  $t_{s,\bullet}$ , the accumulated time of the linear solver (GMRES), and assembly-time,  $t_{a,\bullet}$ , the accumulated time of matrix and vector assembling of the linearized system (18)–(20).

In total, for a full simulation with loading, 18 initialization beats with 1 Newton step, 10 initialization beats with 2 Newton steps, and 2 final beats with a fully converging Newton method the computational costs were around 3.5 h for P1-P0 elements, 13 h for projection stabilized elements, and 17.5 h for MINI elements, see Table 4 for exact values. Here, in addition to GMRES solver and assembly times, also input-output times, the solution of the R-E model governing EP, ODE times, and postprocessing are taken into account. Using a coarser mesh with 45 686 elements and 11 850 nodes tractable computational times could also be achieved on a desktop machine (AMD Ryzen Threadripper 2990X) with 2.5 minutes for one heart beat

Table 3: Summary of electrical and mechanical material parameters.

<i>Passive stress parameters: P1-P0 elements</i>			
$a = 0.1812 \text{ kPa}$ ,	$a_f = 1.3813 \text{ kPa}$ ,	$a_s = 0.5661 \text{ kPa}$ ,	$a_{fs} = 0.0679 \text{ kPa}$ ,
$b = 6.7609 [-]$ ,	$b_f = 29.9854 [-]$ ,	$b_s = 37.8301 [-]$ ,	$b_{fs} = 6.4822 [-]$ .
<i>Passive stress parameters: locking-free elements</i>			
$a = 0.3833 \text{ kPa}$ ,	$a_f = 2.9225 \text{ kPa}$ ,	$a_s = 1.1978 \text{ kPa}$ ,	$a_{fs} = 0.1437 \text{ kPa}$ ,
$b = 5.2278 [-]$ ,	$b_f = 23.1848 [-]$ ,	$b_s = 29.2504 [-]$ ,	$b_{fs} = 5.0121 [-]$ .
<i>Active stress parameters</i>			
$T_{\text{ref}}^{\text{LV}} = 200.0 \text{ mN mm}^{-2}$ ,	$T_{\text{ref}}^{\text{RV}} = 160.0 \text{ mN mm}^{-2}$ ,	$[\text{Ca}^{2+}]_{\text{T50}} = 0.52 \mu\text{mol L}^{-1}$ ,	$\text{TRPN}_{50} = 0.37 [-]$ ,
$n_{\text{TRPN}} = 1.54 [-]$ ,	$k_{\text{TRPN}} = 0.14 \text{ ms}^{-1}$ ,	$n_{\text{xb}} = 3.38 [-]$ ,	$k_{\text{xb}} = 4.9 \times 10^{-3} \text{ ms}^{-1}$ .
<i>Adapted active stress parameters for P1-P0 elements</i>			
$T_{\text{ref}}^{\text{LV}} = 190.0 \text{ mN mm}^{-2}$ ,	$T_{\text{ref}}^{\text{RV}} = 130.0 \text{ mN mm}^{-2}$ .		

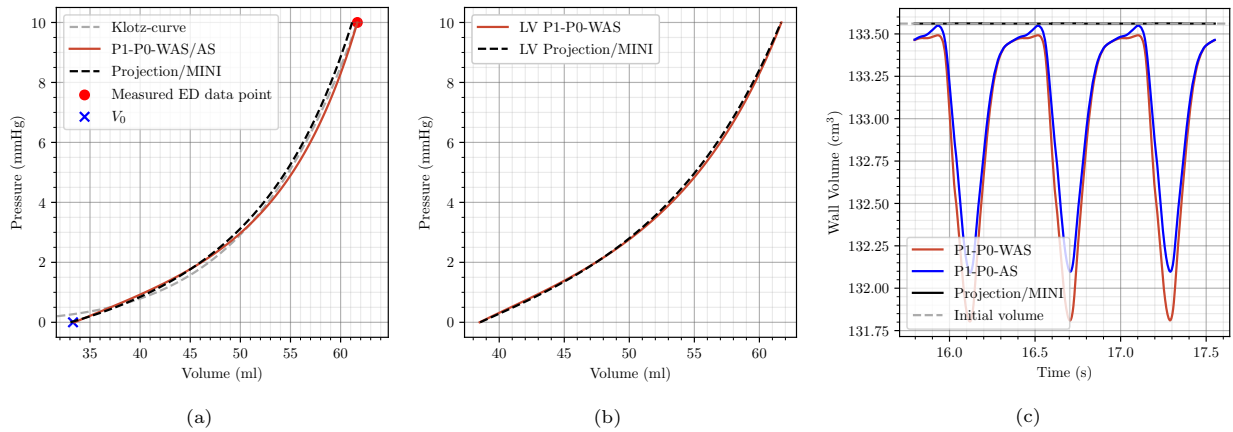


Figure 10: *3D-0D model of the heart*: Passive model calibration and unloading following Marx et al. [96]. (a) An ex-vivo setup was used to calibrate the passive material parameters to fit the EDPVR of Klotz et al. [95]; (b) Calibrated material parameters were used in an in-vivo setup to generate prestress using a backward-displacement scheme. (c) Change in tissue volume over the last three beats.

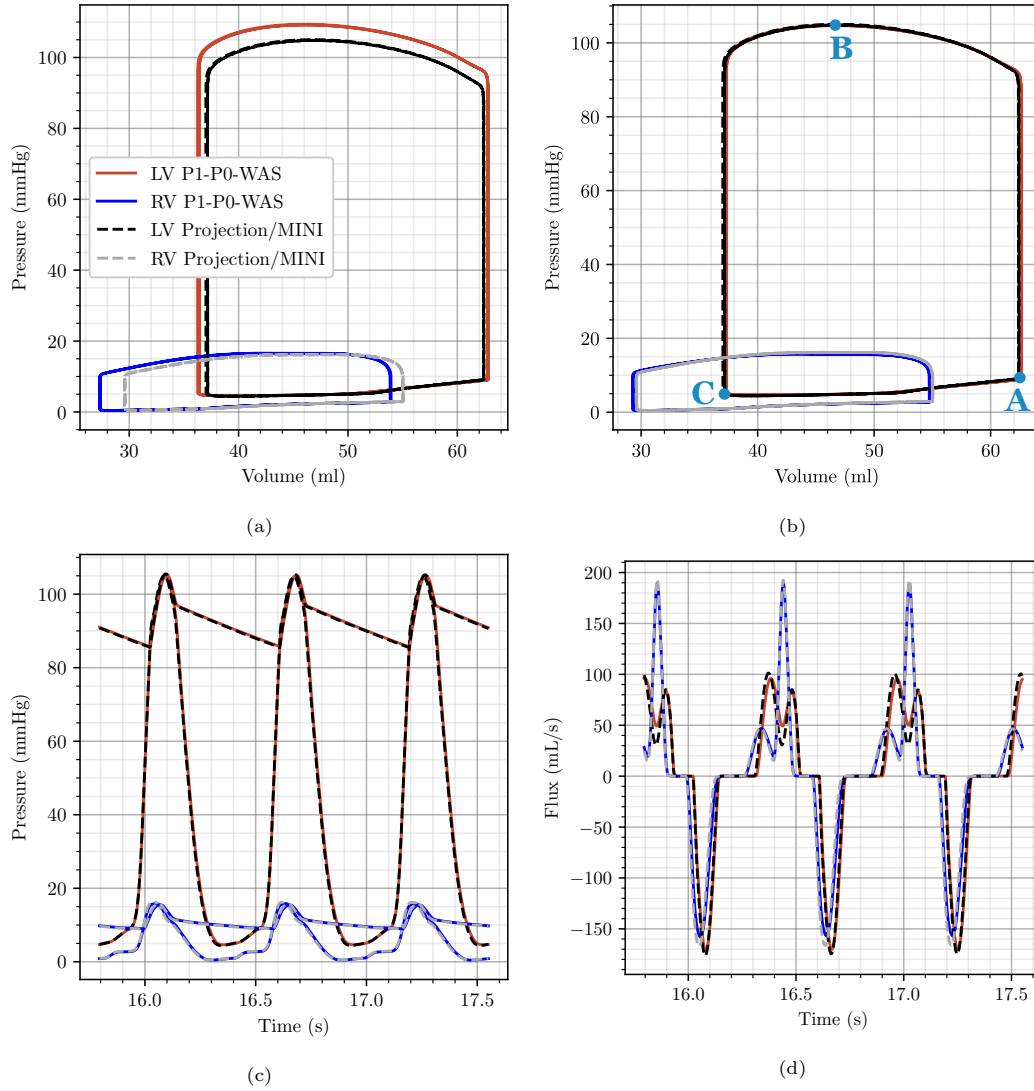


Figure 11: *3D-0D model of the heart*: Plot comparing data traces for the P1-P0-WAS formulation (LV: red lines, RV: blue lines) and for the MINI and stabilized P1-P1 elements (LV: black dashed lines, RV: gray dashed lines). Shown are the last 3 beats of the simulation with (a) same active stress and preload parameters for P1-P0-WAS and locking free elements and (b-d) modified active stress and preload parameters for P1-P0-WAS elements to reach similar PV loops. In particular we show: (a,b) converged PV-loops for both ventricles; (c) pressure trace for the LV and RV and pressure in the respective outflow vessel; (d) in- (negative values) and outflow (positive values) traces of both ventricles. A, B, C mark the time-points for stress plots in Figures 12 and 13.

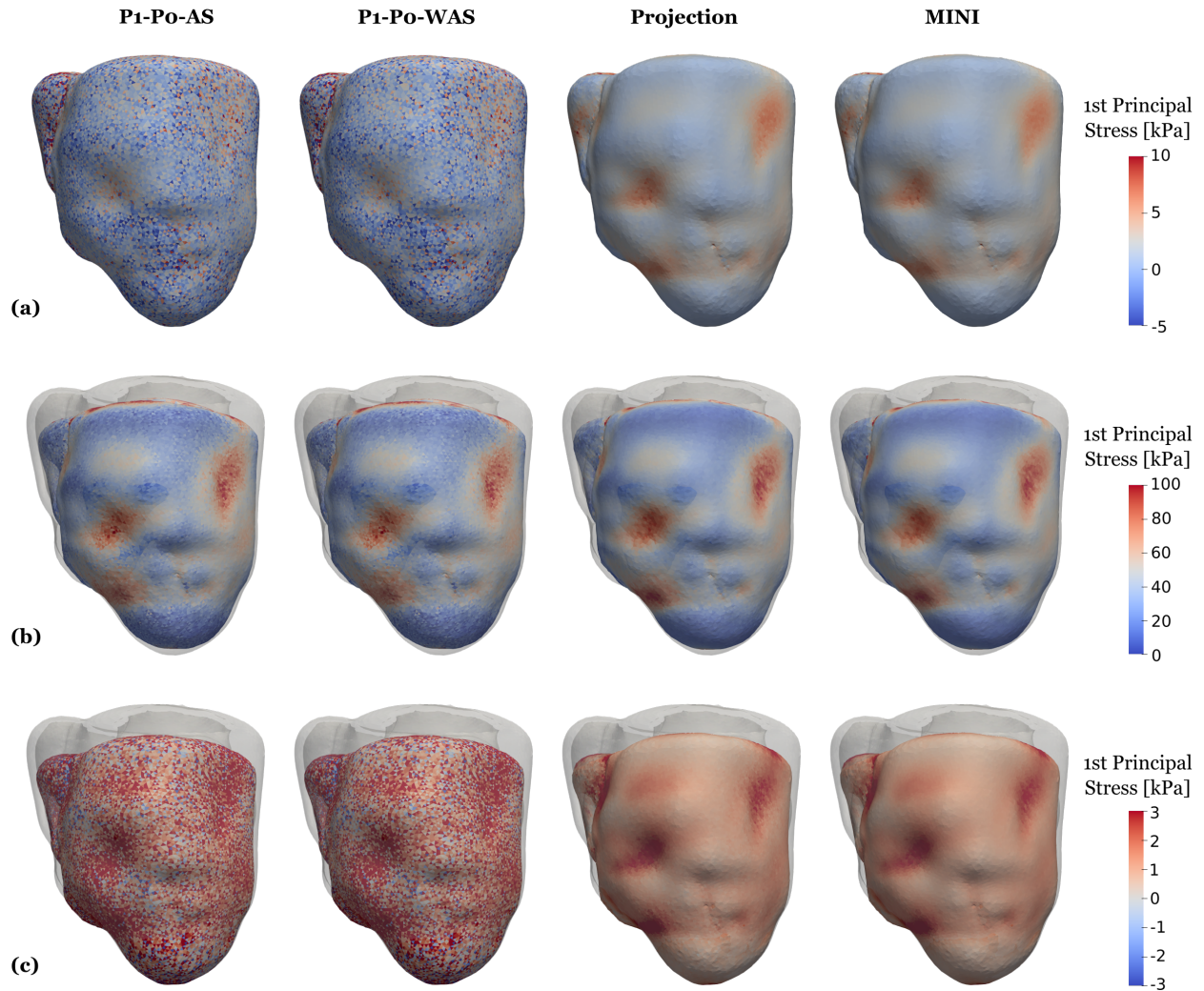


Figure 12: *3D-0D model of the heart*: Snapshots of first principal stress values at end-diastole (first row), peak systole (second row), and at mitral valve opening (third row), see Figure 11 A, B, C for a visualization of the time-points. Gray outlines show the end-diastolic configuration. Compared are P1-P0-WAS elements (first column), stabilized P1-P1 elements (second column), and MINI elements (third column). Shown is total stress as defined stress fields are element-wise and not smoothed.

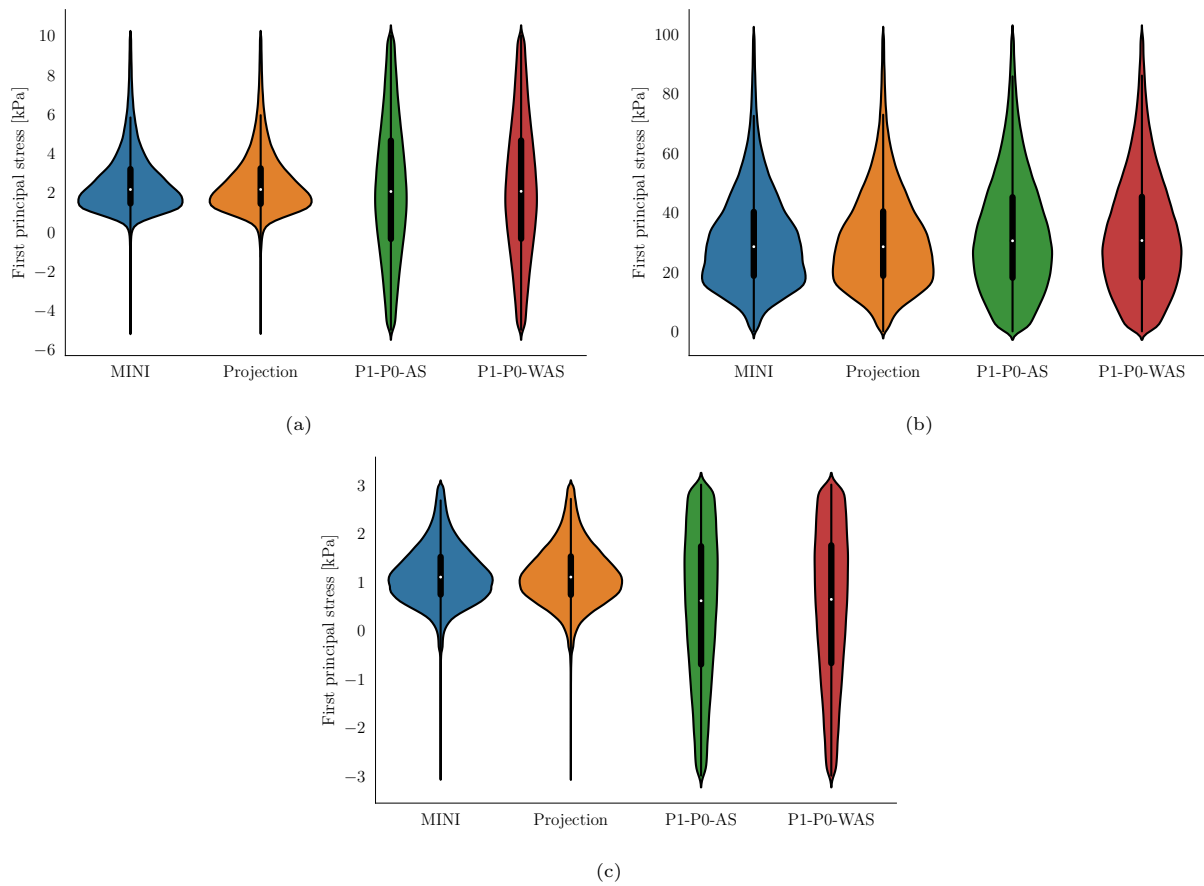


Figure 13: *3D-0D model of the heart*: Violin plots of the first principal stress distribution at (a) end-diastole, (b) peak systole, (c) mitral valve opening.

on 32 cores using P1-P0 elements and 7.15 minutes using locking-free projection stabilized elements. Total computational times on the desktop machine for 30 beats were 94.6 minutes for P1-P0 and 264.4 minutes for projection stabilized elements.

In Figure 14 we show strong scaling properties of the simulation on 16 to 1024 cores of Archer2. Loading and heart beat experiments scale well up to 256 cores for all element types. For 512 and 1024 cores strong scaling efficiency drops markedly due to small local partition sizes ( $< 500$  degrees of freedom per partition).

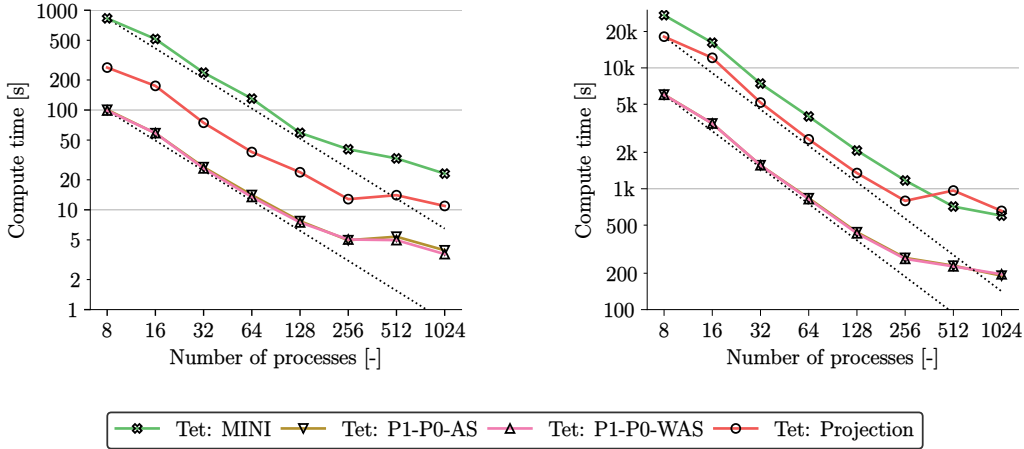


Figure 14: *3D-0D model of the heart*: Strong scaling results for the loading phase (left) and one beat (right). Simulations were performed on 16 to 1024 cores on Archer2.

Type [-]	DOF [-]	$t_{s,1}/t_{a,1}$ [s]	$t_{s,2}/t_{a,2}$ [s]	$t_{s,c}/t_{a,c}$ [s]	$T_{b,1}/T_{b,2}/T_{b,c}$ [s]	$T_{ld}$ [s]	Total [min]
P1-P0-AS	333 702	93.7/93.4	183.6/186.8	938.4/739.0	221.3/438.6/1947.5	7.71	207.2
P1-P0-WAS	333 702	92.1/92.9	181.2/185.8	922.4/739.7	218.7/434.4/1930.4	7.48	205.0
Projection	444 936	573.6/119.1	1289.1/238.2	7479.6/921.3	727.1/1606.0/8694.3	23.8	777.0
MINI	444 936	600.8/495.2	1242.1/990.4	6126.3/3078.8	1181.8/2328.3/9547.5	59.1	1060.5

Table 4: Summary of computational times on 128 cores of Archer2 for the different finite element types. Given are solver, assembly, and total computational times for one beat using one Newton iteration ( $t_{s,1}$ ,  $t_{a,1}$ ) two Newton iterations ( $t_{s,2}$ ,  $t_{a,2}$ ) and a fully converged Newton solution ( $t_{s,c}$ ,  $t_{a,c}$ ).  $T_{b,1}$ ,  $T_{b,2}$ , and  $T_{b,c}$  correspond to the total simulation time per heart beat for one Newton iteration, two Newton iterations, and fully converged Newton scenarios. Timings refer to a single heart beat lasting 0.585s at a time step size of 1 ms. In addition, the times required for the loading phase,  $T_{ld}$ , using 32 load steps and the total simulation times including 0D solution, IO, and postprocessing are presented.

*Discussion.* In this benchmark, we show the most complete model of cardiac EM that is currently available: i) Cardiac electrophysiology was modeled by a reaction-Eikonal model which predicts potential fields with high fidelity even on coarser grids [85]. ii) Cellular dynamics were modeled by the physiological Grandi–Pasqualini–Bers model [86] which is coupled to the Land–Niederer model [87]. This allows for strong coupling, i.e., to account for length and velocity effects on the cytosolic calcium transient, using an approach as described in Augustin et al. [72]. iii) Passive tissue mechanics was modeled by the recent Holzapfel–Ogden type model [84] and active stress according to [89] using a recent approach by Regazzoni and Quarteroni [88] to avoid oscillations. Note that both, passive and active stress computation, account for fiber dispersion, hence, allowing to model the active tension generated by dispersed fibers. iv) Spatially varying Robin boundary conditions were included to model the effect of the pericardium [93]. v) The 3D PDE model was coupled to the physiologically comprehensive 0D closed-loop model CircAdapt of the cardiovascular system. This allows to replicate physiological behaviors under experimental standard protocols altering loading conditions and contractility [62]. vi) Simulations were performed using locking-free finite elements - as presented in this paper - to accurately compute stress distributions.

All computational models of cardiac EM presented in the literature so far, e.g., [82, 62, 98, 99, 100, 101, 102, 27], are missing one or mostly more of the above points. While the importance of model components i) – v) was discussed extensively in references above we could show in this paper that also vi) is necessary to compute accurate stress fields in the tissue. Depending on the application this could be a very critical modeling component, e.g., for the accurate prediction of rupture risks or for the estimation of growth and remodeling based on stress. Note that also for this benchmark we see no substantial difference between simulation outcomes using standard standard P1-P0 and the P1-P0-WAS formulation; both approaches fail to match stress results from gold-standard elements.

While stress fields differ vastly the PV loops computed with locking-free and simple P1-P0 elements are very similar; at least if active and passive tissue parameters are fitted independently for each element type. In particular, passive parameters fitted to the Klotz curve using P1-P0 elements correspond to a softer material. Here, the fitting compensates locking effects to a certain degree. On the other hand, the reference peak tension parameter ( $T_{\text{ref}}^{\bullet}$ ) had to be slightly reduced to reach the same target value as projection stabilized and MINI elements. In this case, the softer passive material and the higher compressibility of the tissue using the penalty term in the P1-P0 formulation are most likely the reasons for higher active stress generation. With these adaptations, PV traces for the different element types are almost identical, see Figure 11. This shows that simple P1-P0 elements can predict most simulation outputs as good as gold standard formulations and are thus adequate for cardiac EM simulations when stresses are not an outcome or critical simulation value. In this case, the computational efficiency of P1-P0 elements might trump the numerical accuracy of locking-free elements.

High resolution EM models require efficient numerical solvers to limit the computational cost that results from a high number of degrees of freedom to capture anatomical details as well as a high number of time steps. Strong scaling characteristics of our EM framework was reported in detail previously [72, 103]. In the present work, we showed that strong scaling is preserved when using locking free elements and a coupling to a 0D model of the circulatory system.

Using the advanced approach presented in this paper, the time needed for the passive filling of the bi-ventricular model of the heart is very low. For the projection stabilized element loading times are less than half a minute on 128 cores@2.25Ghz of Archer2 (Table 4) for the simulation with 444 936 degrees of freedom. Even on 8 cores the passive filling could be achieved within 5 minutes (Figure 14). In comparison, a recent work [19] reports compute times for a similar passive inflation scenario using locking-free elements that were around 162 minutes (203 214 degrees of freedom, 8 cores@2.8Ghz). Fast loading times are crucial for the estimation of the stress-free reference configuration using fixed-point iterations [104, 105].

Computational cost for one heart beat – using grids with a comparable number of elements and nodes but, in general, P1-P0 elements – range from 1.8 to 24 hours in previous studies [82, 99, 100, 101, 102]. In this work, we could show that even with locking-free elements one heart beat can be simulated within 27 minutes on 128 cores of Archer2, see Table 4, and within 11 minutes using 1024 cores, see Figure 14. Still, P1-P0 elements are computationally less expensive with one heart beat in around 7 minutes using 128 cores and 3.2 minutes using 1024 cores. Using a coarser mesh as in [62] fast computational times are also possible on desktop machines with 2.5 minutes for one heart beat on 32 cores using P1-P0 elements and 7.15 minutes using locking-free elements. This computational efficiency is of paramount importance for future parameterization studies where numerous forward simulations have to be carried out to personalize models to patient data.

*Limitations.* First, we set an arbitrary number of 30 heart beats which was more than enough to reach a limit cycle in all experiments. However, an automatic stopping criterion could be used that stops the simulation after reaching the limit cycle. Simulation times could be further reduced by accelerated the convergence to a limit cycle using data-driven 0D emulators [106] or by tuning the 0D CircAdapt model to predict P-V traces from the 3D-0D model in a better fashion, hence, reducing the number of beats needed to a converged solution.

Second, the parameterization of the model has room for improvement. Passive parameters were fitted to the empiric Klotz curve using end-diastolic volume and pressure and active stress was fitted using a target peak pressure value. Other model components such as the reaction-Eikonal model and CircAdapt were not parameterized and we were using default values from the literature. The personalization of the complete model to patient-specific data is not within the scope of this contribution, however, the computational

efficiency of the model is of crucial importance for parameter identification studies that often require a large number of forward simulations.

Third, no independent validation of the model is performed. This could be done by comparing displacements or strains predicted by the model to observations from cine MRI or 3D tagged MRI data, see, e.g., [107, 101, 13]. However, in this work, we focused on showing advantages of locking-free elements for applied simulations using an advanced setup which is necessary to replicate physiological behavior. A rigorous, independent validation against for several patient-specific cases using image data will be the focus of future studies.

Finally, locking-free formulations as presented in this paper require the solution of a block system, which in turn necessitates suitable preconditioning for computational efficiency. This is not a trivial task, however, preconditioners used for simulations in this paper are publicly available through the open-source software framework PETSc.

#### 4. Conclusion

In this study, we introduced stabilization techniques that accelerate simulations of anisotropic materials, in particular, nearly and fully incompressible fiber-reinforced solids such as arterial wall or myocardial tissue. A MINI element formulation and a simple and computationally efficient technique based on a local pressure projection were presented. Both methods were applied for the first time for simulations of anisotropic materials and showed to be an excellent choice when the use of higher order or Taylor–Hood elements is not desired. This is the case, e.g., for detailed, high-resolution problem domains that results in a high number of degrees of freedom. We showed that both approaches are very versatile and can be applied to stationary and transient problems as well as hexahedral and tetrahedral grids without modifications. It is worth noting that all required implementations are purely on the element level, thus, facilitating an inclusion in existing finite element codes. Furthermore, solvers and preconditioners used to solve the linearized block system of equations are available through the open-source software package *PETSc* [74].

We showed the robustness and accuracy of the chosen approaches in two benchmark problems from the literature: first, a thick-walled cylindrical tube representing arterial tissue and second, an ellipsoid representing LV myocardial tissue. Additionally, in a third application of the stabilization approaches, we presented a complex 3D-0D model of the ventricles. This constitutes the first computational EM model of the heart where all components are captured by physiological, state-of-the-art models. We could show that for the first time accurate and physiological cardiovascular simulations are feasible within a clinically tractable time frame.

Computational efficiency of the methods is unprecedented in the literature and the framework shows excellent strong scaling on desktop and HPC architectures. The high versatility of the one-fits-all approach allows the simulation of nearly and fully incompressible fiber-reinforced materials in many different scenarios. Overall, this offers the possibility to perform accurate simulations of biological tissues in clinically tractable time frames, also enabling parameterization studies where numerous forward simulations have to be carried out to personalize models to patient data.

#### Declaration of competing interest

The authors declare that they have no known competing financial interests or personal relationships that could have appeared to influence the work reported in this paper.

#### Acknowledgements

This project has received funding from the European Union’s Horizon 2020 research and innovation programme under the Marie Skłodowska–Curie Action H2020-MSCA-IF-2016 InsiliCardio, GA No. 750835 and under the ERA-NET co-fund action No. 680969 (ERA-CVD SICVALVES, JTC2019) funded by the Austrian Science Fund (FWF), Grant I 4652-B to CMA. Additionally, the research was supported by the Grants F3210-N18 and I2760-B30 from the Austrian Science Fund (FWF) and a BioTechMed Graz flagship award “ILearnHeart” to GP. Further, the project has received funding from the European Union’s Horizon 2020 research and innovation programme under the ERA-LEARN co-fund action No. 811171 (PUSHCART, JTC1\_27) funded by ERA-NET ERACoSysMed to GP.

## References

- [1] A. Grytsan, T. Eriksson, P. Watton, T. Gasser, Growth Description for Vessel Wall Adaptation: A Thick-Walled Mixture Model of Abdominal Aortic Aneurysm Evolution, *Materials* 10 (2017) 994. doi:[10.3390/ma10090994](https://doi.org/10.3390/ma10090994).
- [2] M. Genet, L. C. Lee, B. Baillargeon, J. M. Guccione, E. Kuhl, Modeling Pathologies of Diastolic and Systolic Heart Failure, *Annals of Biomedical Engineering* 44 (2016) 112–127. doi:[10.1007/s10439-015-1351-2](https://doi.org/10.1007/s10439-015-1351-2).
- [3] M. Peirlinck, F. Sahli Costabal, K. L. Sack, J. S. Choy, G. S. Kassab, J. M. Guccione, M. De Beule, P. Segers, E. Kuhl, Using machine learning to characterize heart failure across the scales, *Biomechanics and Modeling in Mechanobiology* 18 (2019) 1987–2001. doi:[10.1007/s10237-019-01190-w](https://doi.org/10.1007/s10237-019-01190-w).
- [4] J. A. Niestrawska, C. M. Augustin, G. Plank, Computational modeling of cardiac growth and remodeling in pressure overloaded hearts—Linking microstructure to organ phenotype, *Acta Biomaterialia* 106 (2020) 34–53. doi:[10.1016/j.actbio.2020.02.010](https://doi.org/10.1016/j.actbio.2020.02.010).
- [5] T. C. Gasser, M. Auer, F. Labruto, J. Swedenborg, J. Roy, Biomechanical rupture risk assessment of abdominal aortic aneurysms: model complexity versus predictability of finite element simulations, *European Journal of Vascular and Endovascular Surgery* 40 (2010) 176–185.
- [6] O. Gültekin, H. Dal, G. A. Holzapfel, A phase-field approach to model fracture of arterial walls: theory and finite element analysis, *Computer methods in applied mechanics and engineering* 312 (2016) 542–566.
- [7] Y. C. Fung, *Biomechanics*, 1, Springer New York, New York, NY, 1990. doi:[10.1007/978-1-4419-6856-2](https://doi.org/10.1007/978-1-4419-6856-2).
- [8] J. M. Guccione, A. D. McCulloch, L. Waldman, Passive material properties of intact ventricular myocardium determined from a cylindrical model (1991).
- [9] G. A. Holzapfel, T. C. Gasser, R. W. Ogden, A new constitutive framework for arterial wall mechanics and a comparative study of material models, *Journal of elasticity and the physical science of solids* 61 (2000) 1–48.
- [10] C. M. Augustin, G. A. Holzapfel, O. Steinbach, Classical and all-floating FETI methods for the simulation of arterial tissues, *International Journal for Numerical Methods in Engineering* 99 (2014) 290–312. doi:[10.1002/nme.4674](https://doi.org/10.1002/nme.4674).
- [11] J. M. Guccione, K. D. Costa, A. D. McCulloch, Finite element stress analysis of left ventricular mechanics in the beating dog heart, *Journal of Biomechanics* 28 (1995) 1167–1177. doi:[10.1016/0021-9290\(94\)00174-3](https://doi.org/10.1016/0021-9290(94)00174-3).
- [12] M. P. Nash, P. J. Hunter, Computational mechanics of the heart, *Journal of elasticity and the physical science of solids* 61 (2000) 113–141.
- [13] K. L. Sack, E. Aliotta, D. B. Ennis, J. S. Choy, G. S. Kassab, J. M. Guccione, T. Franz, Construction and validation of subject-specific biventricular finite-element models of healthy and failing swine hearts from high-resolution DT-MRI, *Frontiers in Physiology* 9 (2018) 1–19.
- [14] I. Babuška, M. Suri, Locking effects in the finite element approximation of elasticity problems, *Numerische Mathematik* 62 (1992) 439–463. doi:[10.1007/BF01396238](https://doi.org/10.1007/BF01396238).
- [15] T. J. R. Hughes, *The Finite Element Method*, Prentice-Hall, Englewood Cliffs, New Jersey, 1987.
- [16] O. C. Zienkiewicz, R. L. Taylor, R. L. Taylor, *The finite element method: solid mechanics, volume 2*, Butterworth-heinemann, 2000.

- [17] P. E. Farrell, L. F. Gatica, B. P. Lamichhane, R. Oyarzúa, R. Ruiz-Baier, Mixed Kirchhoff stress–displacement–pressure formulations for incompressible hyperelasticity, *Computer Methods in Applied Mechanics and Engineering* 374 (2021) 113562. doi:[10.1016/j.cma.2020.113562](https://doi.org/10.1016/j.cma.2020.113562).
- [18] O. Gültekin, H. Dal, G. A. Holzapfel, On the quasi-incompressible finite element analysis of anisotropic hyperelastic materials, *Computational Mechanics* (2018). doi:[10.1007/s00466-018-1602-9](https://doi.org/10.1007/s00466-018-1602-9).
- [19] D. E. Hurtado, P. Zavala, Accelerating cardiac and vessel mechanics simulations: An energy-transform variational formulation for soft-tissue hyperelasticity, *Computer Methods in Applied Mechanics and Engineering* 379 (2021) 113764. doi:<https://doi.org/10.1016/j.cma.2021.113764>.
- [20] J. Schröder, N. Viebahn, D. Balzani, P. Wriggers, A novel mixed finite element for finite anisotropic elasticity; the SKA-element Simplified Kinematics for Anisotropy, *Computer Methods in Applied Mechanics and Engineering* 310 (2016) 475–494. doi:[10.1016/j.cma.2016.06.029](https://doi.org/10.1016/j.cma.2016.06.029).
- [21] P. Flory, Thermodynamic relations for high elastic materials, *Transactions of the Faraday Society* 57 (1961) 829–838.
- [22] R. Glowinski, P. Le Tallec, Augmented Lagrangian and operator-splitting methods in nonlinear mechanics, volume 9, SIAM, 1989.
- [23] J. C. Simo, R. L. Taylor, Quasi-incompressible finite elasticity in principal stretches. continuum basis and numerical algorithms, *Computer methods in applied mechanics and engineering* 85 (1991) 273–310.
- [24] C. Sansour, On the physical assumptions underlying the volumetric-isochoric split and the case of anisotropy, *European Journal of Mechanics, A/Solids* 27 (2008) 28–39. doi:[10.1016/j.euromechsol.2007.04.001](https://doi.org/10.1016/j.euromechsol.2007.04.001).
- [25] J. Helfenstein, M. Jabareen, E. Mazza, S. Govindjee, On non-physical response in models for fiber-reinforced hyperelastic materials, *International Journal of Solids and Structures* 47 (2010) 2056–2061. doi:[10.1016/j.ijsolstr.2010.04.005](https://doi.org/10.1016/j.ijsolstr.2010.04.005).
- [26] J. Schröder, N. Viebahn, D. Balzani, P. Wriggers, A novel mixed finite element for finite anisotropic elasticity; the SKA-element Simplified Kinematics for Anisotropy, *Computer Methods in Applied Mechanics and Engineering* 310 (2016) 475–494. doi:[10.1016/J.CMA.2016.06.029](https://doi.org/10.1016/J.CMA.2016.06.029).
- [27] T. Gerach, S. Schuler, J. Fröhlich, L. Lindner, E. Kovacheva, R. Moss, E. M. Wülfers, G. Seemann, C. Wieners, A. Loewe, Electro-mechanical whole-heart digital twins: A fully coupled multi-physics approach, *Mathematics* 9 (2021) 1247.
- [28] R. C. Kerckhoffs, M. L. Neal, Q. Gu, J. B. Basingthwaite, J. H. Omens, A. D. McCulloch, Coupling of a 3d finite element model of cardiac ventricular mechanics to lumped systems models of the systemic and pulmonic circulation, *Annals of biomedical engineering* 35 (2007) 1–18.
- [29] R. Kerckhoffs, J. Lumens, K. Vernooij, J. Omens, L. Mulligan, T. Delhaas, T. Arts, A. McCulloch, F. Prinzen, Cardiac resynchronization: insight from experimental and computational models, *Progress in biophysics and molecular biology* 97 (2008) 543–561.
- [30] T. P. Usyk, I. J. LeGrice, A. D. McCulloch, Computational model of three-dimensional cardiac electromechanics, *Computing and Visualization in Science* 4 (2002) 249–257. doi:[10.1007/s00791-002-0081-9](https://doi.org/10.1007/s00791-002-0081-9).
- [31] I. Babuška, The finite element method with Lagrangian multipliers, *Numerische Mathematik* (1973). doi:[10.1007/BF01436561](https://doi.org/10.1007/BF01436561).
- [32] F. Brezzi, On the existence, uniqueness and approximation of saddle-point problems arising from Lagrangian multipliers, *Revue française d’automatique, informatique, recherche opérationnelle. Analyse numérique* (1974). doi:[10.1051/m2an/197408R201291](https://doi.org/10.1051/m2an/197408R201291).

- [33] D. Chapelle, K. J. Bathe, The inf-sup test, *Computers and Structures* (1993). doi:[10.1016/0045-7949\(93\)90340-J](https://doi.org/10.1016/0045-7949(93)90340-J).
- [34] C. Taylor, P. Hood, A numerical solution of the Navier-Stokes equations using the finite element technique, *Computers & Fluids* 1 (1973) 73–100. doi:[10.1016/0045-7930\(73\)90027-3](https://doi.org/10.1016/0045-7930(73)90027-3).
- [35] F. Nobile, A. Quarteroni, R. Ruiz-Baier, An active strain electromechanical model for cardiac tissue, *International Journal for Numerical Methods in Biomedical Engineering* 28 (2012) 52–71. doi:[10.1002/cnm.1468](https://doi.org/10.1002/cnm.1468).
- [36] L. P. Franca, T. J. R. Hughes, A. F. D. Loula, I. Miranda, A new family of stable elements for nearly incompressible elasticity based on a mixed Petrov-Galerkin finite element formulation, *Numerische Mathematik* 53 (1988) 123–141. doi:[10.1007/BF01395881](https://doi.org/10.1007/BF01395881).
- [37] T. J. R. Hughes, L. P. Franca, M. Balestra, A new finite element formulation for computational fluid dynamics: V. Circumventing the Babuška–Brezzi condition: a stable Petrov–Galerkin formulation of the stokes problem accommodating equal-order interpolations, *Computer Methods in Applied Mechanics and Engineering* (1986). doi:[10.1016/0045-7825\(86\)90025-3](https://doi.org/10.1016/0045-7825(86)90025-3).
- [38] A. Masud, T. J. Truster, A framework for residual-based stabilization of incompressible finite elasticity: Stabilized formulations and F methods for linear triangles and tetrahedra, *Computer Methods in Applied Mechanics and Engineering* 267 (2013) 359–399. doi:[10.1016/j.cma.2013.08.010](https://doi.org/10.1016/j.cma.2013.08.010).
- [39] S. Rossi, N. Abboud, G. Scovazzi, Implicit finite incompressible elastodynamics with linear finite elements: A stabilized method in rate form, *Computer Methods in Applied Mechanics and Engineering* 311 (2016) 208–249. doi:[10.1016/j.cma.2016.07.015](https://doi.org/10.1016/j.cma.2016.07.015).
- [40] M. Chiumenti, M. Cervera, R. Codina, A mixed three-field FE formulation for stress accurate analysis including the incompressible limit, *Computer Methods in Applied Mechanics and Engineering* 283 (2015) 1095–1116. doi:[10.1016/j.cma.2014.08.004](https://doi.org/10.1016/j.cma.2014.08.004).
- [41] R. Codina, Stabilization of incompressibility and convection through orthogonal sub-scales in finite element methods, *Computer Methods in Applied Mechanics and Engineering* 190 (2000) 1579–1599. doi:[10.1016/S0045-7825\(00\)00254-1](https://doi.org/10.1016/S0045-7825(00)00254-1).
- [42] N. M. Lafontaine, R. Rossi, M. Cervera, M. Chiumenti, Explicit mixed strain-displacement finite element for dynamic geometrically non-linear solid mechanics, *Computational Mechanics* 55 (2015) 543–559. doi:[10.1007/s00466-015-1121-x](https://doi.org/10.1007/s00466-015-1121-x).
- [43] F. Auricchio, L. B. da Veiga, C. Lovadina, A. Reali, A stability study of some mixed finite elements for large deformation elasticity problems, *Computer Methods in Applied Mechanics and Engineering* 194 (2005) 1075–1092.
- [44] F. Auricchio, L. B. Da Veiga, C. Lovadina, A. Reali, The importance of the exact satisfaction of the incompressibility constraint in nonlinear elasticity: mixed fems versus nurbs-based approximations, *Computer Methods in Applied Mechanics and Engineering* 199 (2010) 314–323.
- [45] R. A. Boerboom, N. J. Driessen, C. V. Bouten, J. M. Huyghe, F. P. Baaijens, Finite element model of mechanically induced collagen fiber synthesis and degradation in the aortic valve, *Annals of Biomedical Engineering* 31 (2003) 1040–1053.
- [46] S. Göktepe, S. Acharya, J. Wong, E. Kuhl, Computational modeling of passive myocardium, *International Journal for Numerical Methods in Biomedical Engineering* 27 (2011) 1–12.
- [47] J. A. Weiss, B. N. Maker, S. Govindjee, Finite element implementation of incompressible, transversely isotropic hyperelasticity, *Computer methods in applied mechanics and engineering* 135 (1996) 107–128.
- [48] A. Zdunek, W. Rachowicz, T. Eriksson, Nearly incompressible and nearly inextensible finite hyperelasticity, *Computer Methods in Applied Mechanics and Engineering* (2014) 1–42. doi:[10.1016/j.cma.2014.08.008](https://doi.org/10.1016/j.cma.2014.08.008).

- [49] D. N. Arnold, F. Brezzi, M. Fortin, A stable finite element for the stokes equations, *Calcolo* 21 (1984) 337–344. doi:[10.1007/bf02576171](https://doi.org/10.1007/bf02576171).
- [50] T. H. Ong, C. E. Heaney, C.-K. Lee, G. Liu, H. Nguyen-Xuan, On stability, convergence and accuracy of bES-FEM and bFS-FEM for nearly incompressible elasticity 285 (2015) 315–345. doi:[10.1016/j.cma.2014.10.022](https://doi.org/10.1016/j.cma.2014.10.022).
- [51] C.-K. Lee, L. A. Mihai, J. S. Hale, P. Kerfriden, S. P. Bordas, Strain smoothing for compressible and nearly-incompressible finite elasticity 182 (2017) 540–555. doi:[10.1016/j.compstruc.2016.05.004](https://doi.org/10.1016/j.compstruc.2016.05.004).
- [52] C. R. Dohrmann, P. B. Bochev, A stabilized finite element method for the Stokes problem based on polynomial pressure projections, *International Journal for Numerical Methods in Fluids* 46 (2004) 183–201. doi:[10.1002/flid.752](https://doi.org/10.1002/flid.752).
- [53] J. M. Ball, Convexity conditions and existence theorems in nonlinear elasticity, *Archive for Rational Mechanics and Analysis* 63 (1976) 337–403. doi:[10.1007/BF00279992](https://doi.org/10.1007/BF00279992).
- [54] P. G. Ciarlet, *The finite element method for elliptic problems*, volume 40, Siam, 2002.
- [55] S. Rossi, N. Abboud, G. Scovazzi, Implicit finite incompressible elastodynamics with linear finite elements: A stabilized method in rate form, *Computer Methods in Applied Mechanics and Engineering* 311 (2016) 208–249. doi:[10.1016/j.cma.2016.07.015](https://doi.org/10.1016/j.cma.2016.07.015).
- [56] S. Hartmann, P. Neff, Polyconvexity of generalized polynomial-type hyperelastic strain energy functions for near-incompressibility, *International journal of solids and structures* 40 (2003) 2767–2791.
- [57] S. Doll, K. Schweizerhof, On the Development of Volumetric Strain Energy Functions, *Journal of Applied Mechanics* 67 (2000) 17. doi:[10.1115/1.321146](https://doi.org/10.1115/1.321146).
- [58] T. Sussman, K.-J. Bathe, A finite element formulation for nonlinear incompressible elastic and inelastic analysis, *Computers & Structures* 26 (1987) 357–409.
- [59] S. N. Atluri, E. Reissner, On the formulation of variational theorems involving volume constraints, *Computational Mechanics* 5 (1989) 337–344.
- [60] J. C. Simo, R. L. Taylor, P. Wriggers, A note on finite-element implementation of pressure boundary loading, *Communications in Applied Numerical Methods* 7 (1991) 513–525. doi:[10.1002/cnm.1630070703](https://doi.org/10.1002/cnm.1630070703).
- [61] U. Brink, E. Stein, On some mixed finite element methods for incompressible and nearly incompressible finite elasticity, *Computational Mechanics* 19 (1996) 105–119.
- [62] C. M. Augustin, M. A. Gsell, E. Karabelas, E. Willemen, F. W. Prinzen, J. Lumens, E. J. Vigmond, G. Plank, A computationally efficient physiologically comprehensive 3D–0D closed-loop model of the heart and circulation, *Computer Methods in Applied Mechanics and Engineering* 386 (2021) 114092. doi:[10.1016/j.cma.2021.114092](https://doi.org/10.1016/j.cma.2021.114092).
- [63] E. Karabelas, G. Haase, G. Plank, C. M. Augustin, Versatile stabilized finite element formulations for nearly and fully incompressible solid mechanics, *Computational Mechanics* 65 (2020) 193–215. doi:[10.1007/s00466-019-01760-w](https://doi.org/10.1007/s00466-019-01760-w).
- [64] P. Knabner, S. Korotov, G. Summ, Conditions for the invertibility of the isoparametric mapping for hexahedral finite elements, *Finite Elements in Analysis and Design* 40 (2003) 159 – 172. doi:[https://doi.org/10.1016/S0168-874X\(02\)00196-8](https://doi.org/10.1016/S0168-874X(02)00196-8).
- [65] J. Cante, C. Dávalos, J. A. Hernández, J. Oliver, P. Jonsén, G. Gustafsson, H.-Å. Häggblad, PFEM-based modeling of industrial granular flows, *Computational Particle Mechanics* 1 (2014) 47–70. doi:[10.1007/s40571-014-0004-9](https://doi.org/10.1007/s40571-014-0004-9).

- [66] J. M. Rodriguez, J. M. Carbonell, J. C. Cante, J. Oliver, The particle finite element method (PFEM) in thermo-mechanical problems, *International Journal for Numerical Methods in Engineering* 107 (2016) 733–785. doi:[10.1002/nme.5186](https://doi.org/10.1002/nme.5186).
- [67] F. Brezzi, M.-O. Bristeau, L. P. Franca, M. Mallet, G. Rogé, A relationship between stabilized finite element methods and the galerkin method with bubble functions, *Computer Methods in Applied Mechanics and Engineering* 96 (1992) 117–129. doi:[10.1016/0045-7825\(92\)90102-p](https://doi.org/10.1016/0045-7825(92)90102-p).
- [68] D. Boffi, F. Brezzi, M. Fortin, *Mixed finite element methods and applications*, Springer, 2013.
- [69] J. M. Guccione, K. D. Costa, A. D. McCulloch, Finite element stress analysis of left ventricular mechanics in the beating dog heart, *Journal of Biomechanics* 28 (1995) 1167–1177. doi:[10.1016/0021-9290\(94\)00174-3](https://doi.org/10.1016/0021-9290(94)00174-3).
- [70] C. Sansour, On the physical assumptions underlying the volumetric-isochoric split and the case of anisotropy, *European Journal of Mechanics - A/Solids* 27 (2008) 28 – 39. doi:[10.1016/j.euromechsol.2007.04.001](https://doi.org/10.1016/j.euromechsol.2007.04.001).
- [71] J. Helfenstein, M. Jabareen, E. Mazza, S. Govindjee, On non-physical response in models for fiber-reinforced hyperelastic materials, *International Journal of Solids and Structures* 47 (2010) 2056 – 2061. doi:[10.1016/j.ijsolstr.2010.04.005](https://doi.org/10.1016/j.ijsolstr.2010.04.005).
- [72] C. M. Augustin, A. Neic, M. Liebmann, A. J. Prassl, S. A. Niederer, G. Haase, G. Plank, Anatomically accurate high resolution modeling of cardiac electromechanics: a strongly scalable algebraic multigrid solver method for non-linear deformation, *J Comput Phys* 305 (2016) 622–646. doi:[10.1016/j.jcp.2015.10.045](https://doi.org/10.1016/j.jcp.2015.10.045).
- [73] E. Vigmond, R. Weber dos Santos, A. Prassl, M. Deo, G. Plank, Solvers for the cardiac bidomain equations, *Prog Biophys Mol Biol* 96 (2008) 3–18.
- [74] S. Balay, S. Abhyankar, M. F. Adams, J. Brown, P. Brune, K. Buschelman, L. Dalcin, A. Dener, V. Eijkhout, W. D. Gropp, D. Kaushik, M. G. Knepley, D. A. May, L. C. McInnes, R. T. Mills, T. Munson, K. Rupp, P. Sanan, B. F. Smith, S. Zampini, H. Zhang, H. Zhang, *PETSc Users Manual*, Technical Report ANL-95/11 - Revision 3.10, Argonne National Laboratory, 2018.
- [75] D. A. May, P. Sanan, K. Rupp, M. G. Knepley, B. F. Smith, Extreme-scale multigrid components within petsc, in: *Proceedings of the Platform for Advanced Scientific Computing Conference*, 2016, pp. 1–12.
- [76] O. Gültekin, H. Dal, G. A. Holzapfel, On the quasi-incompressible finite element analysis of anisotropic hyperelastic materials, *Computational Mechanics* 63 (2019) 443–453. doi:[10.1007/s00466-018-1602-9](https://doi.org/10.1007/s00466-018-1602-9).
- [77] É. Chamberland, A. Fortin, M. Fortin, Comparison of the performance of some finite element discretizations for large deformation elasticity problems, *Computers & Structures* 88 (2010) 664–673. doi:[10.1016/j.compstruc.2010.02.007](https://doi.org/10.1016/j.compstruc.2010.02.007).
- [78] S. Land, V. Gurev, S. Arens, C. M. Augustin, L. Baron, R. Blake, C. Bradley, S. Castro, A. Crozier, M. Favino, T. E. Fastl, T. Fritz, H. Gao, A. Gizzi, B. E. Griffith, D. E. Hurtado, R. Krause, X. Luo, M. P. Nash, S. Pezzuto, G. Plank, S. Rossi, D. Ruprecht, G. Seemann, N. P. Smith, J. Sundnes, J. J. Rice, N. Trayanova, D. Wang, Z. Jenny Wang, S. A. Niederer, Verification of cardiac mechanics software: benchmark problems and solutions for testing active and passive material behaviour, *Proceedings of the Royal Society A: Mathematical, Physical and Engineering Science* 471 (2015) 20150641. doi:[10.1098/rspa.2015.0641](https://doi.org/10.1098/rspa.2015.0641).
- [79] G. A. Holzapfel, R. W. Ogden, Constitutive modelling of passive myocardium: a structurally based framework for material characterization, *Phil. Trans. R. Soc. A* 367 (2009) 3445–75. doi:[10.1098/rsta.2009.0091](https://doi.org/10.1098/rsta.2009.0091).

- [80] D. Guan, F. Ahmad, P. Theobald, S. Soe, X. Luo, H. Gao, On the AIC-based model reduction for the general Holzapfel–Ogden myocardial constitutive law, *Biomechanics and Modeling in Mechanobiology* 18 (2019) 1213–1232.
- [81] G. Sommer, A. J. Schriefl, M. Andrä, M. Sacherer, C. Viertler, H. Wolinski, G. A. Holzapfel, Biomechanical properties and microstructure of human ventricular myocardium, *Acta Biomaterialia* 24 (2015) 172–192.
- [82] V. Gurev, P. Pathmanathan, J.-L. Fattibert, H.-F. Wen, J. Magerlein, R. a. Gray, D. F. Richards, J. J. Rice, A high-resolution computational model of the deforming human heart, *Biomechanics and Modeling in Mechanobiology* 14 (2015) 829–849. doi:[10.1007/s10237-014-0639-8](https://doi.org/10.1007/s10237-014-0639-8).
- [83] A. Logg, K.-A. Mardal, G. Wells, Automated solution of differential equations by the finite element method: The FEniCS book, volume 84, Springer Science & Business Media, 2012.
- [84] O. Gültekin, G. Sommer, G. A. Holzapfel, An orthotropic viscoelastic model for the passive myocardium: continuum basis and numerical treatment, *Computer methods in biomechanics and biomedical engineering* 19 (2016) 1647–1664.
- [85] A. Neic, F. O. Campos, A. J. Prassl, S. A. Niederer, M. J. Bishop, E. J. Vigmond, G. Plank, Efficient computation of electrograms and ECGs in human whole heart simulations using a reaction-eikonal model, *Journal of Computational Physics* 346 (2017) 191–211.
- [86] E. Grandi, F. S. Pasqualini, D. M. Bers, A novel computational model of the human ventricular action potential and Ca transient, *Journal of Molecular and Cellular Cardiology* 48 (2010) 112–121. doi:[10.1016/j.yjmcc.2009.09.019](https://doi.org/10.1016/j.yjmcc.2009.09.019).
- [87] S. Land, S. A. Niederer, J. M. Aronsen, E. K. S. Espe, L. Zhang, W. E. Louch, I. Sjaastad, O. M. Sejersted, N. P. Smith, An analysis of deformation-dependent electromechanical coupling in the mouse heart., *The Journal of physiology* 590 (2012) 4553–69. doi:[10.1113/jphysiol.2012.231928](https://doi.org/10.1113/jphysiol.2012.231928).
- [88] F. Regazzoni, A. Quarteroni, An oscillation-free fully staggered algorithm for velocity-dependent active models of cardiac mechanics, *Computer Methods in Applied Mechanics and Engineering* 373 (2021) 113506. doi:[10.1016/j.cma.2020.113506](https://doi.org/10.1016/j.cma.2020.113506).
- [89] T. S. E. Eriksson, A. J. Prassl, G. Plank, G. A. Holzapfel, Modeling the dispersion in electromechanically coupled myocardium, *International Journal for Numerical Methods in Biomedical Engineering* 29 (2013) 1267–1284.
- [90] C. Kadapa, W. Dettmer, D. Perić, On the advantages of using the first-order generalised-alpha scheme for structural dynamic problems 193 (2017) 226–238. doi:[10.1016/j.compstruc.2017.08.013](https://doi.org/10.1016/j.compstruc.2017.08.013).
- [91] J. D. Bayer, R. C. Blake, G. Plank, N. A. Trayanova, A novel rule-based algorithm for assigning myocardial fiber orientation to computational heart models, *Annals of Biomedical Engineering* 40 (2012) 2243–2254.
- [92] D. D. Streeter, H. M. Spotnitz, D. P. Patel, J. Ross, E. H. Sonnenblick, Fiber orientation in the canine left ventricle during diastole and systole., *Circulation research* (1969).
- [93] M. Strocchi, M. A. Gsell, C. M. Augustin, O. Razeghi, C. H. Roney, A. J. Prassl, E. J. Vigmond, J. M. Behar, J. S. Gould, C. A. Rinaldi, M. J. Bishop, G. Plank, S. A. Niederer, Simulating ventricular systolic motion in a four-chamber heart model with spatially varying robin boundary conditions to model the effect of the pericardium, *Journal of Biomechanics* 101 (2020) 109645. doi:[10.1016/j.jbiomech.2020.109645](https://doi.org/10.1016/j.jbiomech.2020.109645).
- [94] J. Walmsley, T. Arts, N. Derval, P. Bordachar, H. Cochet, S. Ploux, F. W. Prinzen, T. Delhaas, J. Lumens, Fast Simulation of Mechanical Heterogeneity in the Electrically Asynchronous Heart Using the MultiPatch Module, *PLOS Computational Biology* 11 (2015) e1004284.

- [95] S. Klotz, M. L. Dickstein, D. Burkhoff, A computational method of prediction of the end-diastolic pressure–volume relationship by single beat, *Nature Protocols* 2 (2007) 2152–2158.
- [96] L. Marx, J. A. Niestrawska, M. A. Gsell, F. Caforio, G. Plank, C. M. Augustin, Efficient identification of myocardial material parameters and the stress-free reference configuration for patient-specific human heart models, *arXiv preprint arXiv:2101.04411* (2021).
- [97] P. Deuffhard, *Newton Methods for Nonlinear Problems: Affine Invariance and Adaptive Algorithms*, volume 35, Springer Science & Business Media, 2011.
- [98] R. Piersanti, F. Regazzoni, M. Salvador, A. F. Corno, L. Dede', C. Vergara, A. Quarteroni, 3d-0d closed-loop model for the simulation of cardiac biventricular electromechanics, 2021. [arXiv:2108.01907](https://arxiv.org/abs/2108.01907).
- [99] T. Kariya, T. Washio, J. ichi Okada, M. Nakagawa, M. Watanabe, Y. Kadooka, S. Sano, R. Nagai, S. Sugiura, T. Hisada, Personalized Perioperative Multi-scale, Multi-physics Heart Simulation of Double Outlet Right Ventricle, *Annals of Biomedical Engineering* 48 (2020) 1740–1750.
- [100] M. Hirschvogel, M. Bassilious, L. Jagschies, S. M. Wildhirt, M. W. Gee, A monolithic 3D-0D coupled closed-loop model of the heart and the vascular system: Experiment-based parameter estimation for patient-specific cardiac mechanics, *International Journal for Numerical Methods in Biomedical Engineering* 33 (2017).
- [101] M. R. Pfaller, J. M. Hörmann, M. Weigl, A. Nagler, R. Chabiniok, C. Bertoglio, W. A. Wall, The importance of the pericardium for cardiac biomechanics: from physiology to computational modeling, *Biomechanics and Modeling in Mechanobiology* 18 (2019) 503–529.
- [102] Z. J. Wang, A. Santiago, X. Zhou, L. Wang, F. Margara, F. Levrero-Florencio, A. Das, C. Kelly, E. Dallarmellina, M. Vazquez, B. Rodriguez, Human biventricular electromechanical simulations on the progression of electrocardiographic and mechanical abnormalities in post-myocardial infarction, *Europace* 23 (2021) I143–I152.
- [103] E. Karabelas, M. A. F. Gsell, C. M. Augustin, L. Marx, A. Neic, A. J. Prassl, L. Goubergrits, T. Kuehne, G. Plank, Towards a Computational Framework for Modeling the Impact of Aortic Coarctations Upon Left Ventricular Load, *Frontiers in Physiology* 9 (2018) 1–20.
- [104] M. Sellier, An iterative method for the inverse elasto-static problem, *Journal of Fluids and Structures* 27 (2011) 1461–1470.
- [105] M. K. Rausch, M. Genet, J. D. Humphrey, An augmented iterative method for identifying a stress-free reference configuration in image-based biomechanical modeling, *Journal of Biomechanics* 58 (2017) 227–231.
- [106] F. Regazzoni, A. Quarteroni, Accelerating the convergence to a limit cycle in 3d cardiac electromechanical simulations through a data-driven 0d emulator, *Computers in Biology and Medicine* 135 (2021) 104641. doi:<https://doi.org/10.1016/j.compbiomed.2021.104641>.
- [107] A. V. S. Ponnaluri, I. A. Verzhbinsky, J. D. Eldredge, A. Garfinkel, D. B. Ennis, L. E. Perotti, Model of Left Ventricular Contraction: Validation Criteria and Boundary Conditions, in: *Lecture Notes in Computer Science*, volume 11504 LNCS, Springer International Publishing, 2019, pp. 294–303.
- [108] G. A. Holzapfel, *Nonlinear solid mechanics: A continuum approach for engineering*, John Wiley & Sons Ltd, Chichester, 2000. doi:[10.1023/A:1020843529530](https://doi.org/10.1023/A:1020843529530).
- [109] P. Wriggers, *Nonlinear Finite Element Methods*, Springer Berlin Heidelberg, Berlin, Heidelberg, 2008. doi:[10.1007/978-3-540-71001-1](https://doi.org/10.1007/978-3-540-71001-1).

## Appendix A. Linearization

We will give a short summary of the linearization of a cavity volume  $V_{\text{CAV}}$  defined by

$$V_{\text{CAV}} := \frac{1}{3} \int_{\Gamma_{\text{CAV}}} \mathbf{x} \cdot \mathbf{n} \, ds_{\mathbf{x}}.$$

Using Nanson's formula and  $\mathbf{x} = \mathbf{X} + \mathbf{u}$  we can rewrite this as

$$V_{\text{CAV}} = \frac{1}{3} \int_{\Gamma_{\text{CAV},0}} (\mathbf{X} + \mathbf{u}) \cdot J \mathbf{F}^{-\top} \mathbf{N} \, ds_{\mathbf{X}}$$

Using the known linearizations

$$\frac{\partial J}{\partial \mathbf{F}} : \text{Grad } \Delta \mathbf{u} = J \mathbf{F}^{-\top} : \text{Grad } \Delta \mathbf{u} \quad (\text{A.1})$$

$$\frac{\partial \mathbf{F}^{-\top}}{\partial \mathbf{F}} : \text{Grad } \Delta \mathbf{u} = -\mathbf{F}^{-\top} (\text{Grad } \Delta \mathbf{u})^{\top} \mathbf{F}^{-\top} \quad (\text{A.2})$$

we can calculate the linearization around  $\Delta \mathbf{u}$  as

$$d_k(\Delta \mathbf{u}) := D_{\Delta \mathbf{u}} V_{\text{CAV}} = D_{\Delta \mathbf{u}} \frac{1}{3} \int_{\Gamma_{\text{CAV}}} \mathbf{x} \cdot \mathbf{n} \, ds_{\mathbf{x}} \quad (\text{A.3})$$

$$= D_{\Delta \mathbf{u}} \frac{1}{3} \int_{\Gamma_{\text{CAV},0}} J(\mathbf{X} + \mathbf{u}) \cdot \mathbf{F}^{-\top} \mathbf{N} \, ds_{\mathbf{X}} \quad (\text{A.4})$$

$$= \frac{1}{3} \int_{\Gamma_{\text{CAV},0}} J(\mathbf{F}^{-\top} : \text{Grad } \Delta \mathbf{u}) \mathbf{x} \cdot \mathbf{F}^{-\top} \mathbf{N} \, ds_{\mathbf{X}} \quad (\text{A.5})$$

$$- \frac{1}{3} \int_{\Gamma_{\text{CAV},0}} J \mathbf{x} \cdot \mathbf{F}^{-\top} (\text{Grad } \Delta \mathbf{u})^{\top} \mathbf{F}^{-\top} \mathbf{N} \, ds_{\mathbf{X}} \quad (\text{A.6})$$

$$+ \frac{1}{3} \int_{\Gamma_{\text{CAV},0}} J \Delta \mathbf{u} \cdot \mathbf{F}^{-\top} \mathbf{N} \, ds_{\mathbf{X}} \quad (\text{A.7})$$

## Appendix B. Static Condensation for Inhomogeneous Neumann Boundary Condition

While homogenous Neumann boundary conditions don't alter the process of static condensation, the procedure needs to be adapted to for inhomogenous ones. First, looking at the definition of the nonlinear residual  $R_{\text{vol}}$  in (5) we see that this can be split as

$$R_{\text{vol}} = R_{\text{vol},\Omega_0} + R_{\text{vol},\Gamma_{N,0}}$$

where  $R_{\text{vol},\Omega_0}$  holds all the terms coming from integration over the domain  $\Omega_0$  and  $R_{\text{vol},\Gamma_{N,0}}$  holds all the terms coming from integration over the Neumann surfaces. Next, note that the bubble functions  $\hat{\psi}_{\text{B}}$  for tetrahedral elements as well as their hexahedral counterparts  $\hat{\psi}_{\text{B},1}, \hat{\psi}_{\text{B},2}$  have compact support in the finite element interior. However, the respective gradients don't vanish on the finite element boundary. Consider an arbitrary finite element  $K \in \mathcal{T}_h$  with  $K \cap \Gamma_{N,0} \neq \emptyset$ . The gradient of a bubble function occurs in bilinear-form  $a_{\Gamma,k}$  in (17), for the argument  $\Delta \mathbf{u} \in V_h$ . This yields a non-zero contribution to the element-stiffness-matrix, whereas there is no contribution from  $R_{\text{vol},\Gamma_{N,0}}$  to the total element residual vector. Using the decomposition of local degrees of freedom into *exterior*, E and *interior*, I it follows that the local block system can be written in the following form

$$\begin{pmatrix} \mathbf{K}_{\text{EE}} + \mathbf{K}_{\Gamma,\text{EE}} & \mathbf{K}_{\text{EI}} + \mathbf{K}_{\Gamma,\text{EI}} & \mathbf{B}_{\text{E}} \\ \mathbf{K}_{\text{IE}} & \mathbf{K}_{\text{II}} & \mathbf{B}_{\text{I}} \\ \mathbf{C}_{\text{E}} & \mathbf{C}_{\text{I}} & \mathbf{D}_{\text{E}} \end{pmatrix} \begin{pmatrix} \Delta \underline{u}_{\text{E}} \\ \Delta \underline{u}_{\text{I}} \\ \Delta \underline{p}_{\text{E}} \end{pmatrix} = \begin{pmatrix} -\underline{R}_{\text{vol},\text{E}} - R_{\text{vol},\Gamma,\text{E}} \\ -\underline{R}_{\text{vol},\text{I}} \\ -\underline{R}_{\text{inc},\text{E}} \end{pmatrix}.$$

The interior degrees of freedom can be statically condensed. On element level this leads to the static condensed system

$$\underbrace{\begin{pmatrix} \widetilde{\mathbf{K}} & \widetilde{\mathbf{B}} \\ \widetilde{\mathbf{C}} & \widetilde{\mathbf{D}} \end{pmatrix}}_{:=\widetilde{\mathbf{A}}} \begin{pmatrix} \Delta \underline{u}_E \\ \Delta \underline{p}_E \end{pmatrix} + \underbrace{\begin{pmatrix} \widetilde{\mathbf{K}}_\Gamma & \widetilde{\mathbf{B}}_\Gamma \\ \mathbf{0} & \mathbf{0} \end{pmatrix}}_{:=\widetilde{\mathbf{A}}_\Gamma} \begin{pmatrix} \Delta \underline{u}_E \\ \Delta \underline{p}_E \end{pmatrix} = \underbrace{\begin{pmatrix} -\widetilde{\underline{R}}_{\text{vol}} \\ -\widetilde{\underline{R}}_{\text{inc}} \end{pmatrix}}_{:=\underline{\mathbf{R}}} + \underbrace{\begin{pmatrix} -\widetilde{\underline{R}}_{\Gamma, \text{upper}} \\ \underline{\mathbf{0}} \end{pmatrix}}_{:=\underline{\mathbf{R}}_\Gamma},$$

where

$$\begin{aligned} \widetilde{\mathbf{K}} &:= \mathbf{K}_{\text{EE}} - \mathbf{K}_{\text{EI}} \mathbf{K}_{\text{II}}^{-1} \mathbf{K}_{\text{IE}}, & \widetilde{\mathbf{B}} &:= \mathbf{B}_E - \mathbf{K}_{\text{EI}} \mathbf{K}_{\text{II}}^{-1} \mathbf{B}_I, \\ \widetilde{\mathbf{C}} &:= \mathbf{C}_E - \mathbf{C}_I \mathbf{K}_{\text{II}}^{-1} \mathbf{K}_{\text{IE}}, & \widetilde{\mathbf{D}} &:= \mathbf{D}_E - \mathbf{C}_I \mathbf{K}_{\text{II}}^{-1} \mathbf{B}_I, \\ \widetilde{\mathbf{K}}_\Gamma &:= \mathbf{K}_{\Gamma, \text{EE}} - \mathbf{K}_{\Gamma, \text{EI}} \mathbf{K}_{\text{II}}^{-1} \mathbf{K}_{\text{IE}}, & \widetilde{\mathbf{B}}_\Gamma &:= -\mathbf{K}_{\Gamma, \text{EI}} \mathbf{K}_{\text{II}}^{-1} \mathbf{B}_I, \\ \widetilde{\underline{R}}_{\text{vol}} &:= \underline{R}_{\text{vol}, E} - \mathbf{K}_{\text{EI}} \mathbf{K}_{\text{II}}^{-1} \underline{R}_{\text{vol}, I}, & \widetilde{\underline{R}}_{\Gamma, \text{vol}} &:= \underline{R}_{\Gamma, E} - \mathbf{K}_{\Gamma, \text{EI}} \mathbf{K}_{\text{II}}^{-1} \underline{R}_{\text{vol}, I}, \\ \widetilde{\underline{R}}_{\text{inc}} &:= \underline{R}_{\text{inc}, E} - \mathbf{C}_I \mathbf{K}_{\text{II}}^{-1} \underline{R}_{\text{inc}, I}. \end{aligned}$$

The individual element matrices/vectors  $\widetilde{\mathbf{A}}$ ,  $\widetilde{\mathbf{A}}_\Gamma$ ,  $\widetilde{\underline{R}}$ , and  $\widetilde{\underline{R}}_\Gamma$  can be assembled into a global stiffness matrix through loops over volume elements and surface elements respectively. In the case of an attached circulatory system a static condensation can be performed in an analogous way

$$\begin{pmatrix} \mathbf{K}_{\text{EE}} + \mathbf{K}_{\Gamma, \text{EE}} & \mathbf{K}_{\text{EI}} + \mathbf{K}_{\Gamma, \text{EI}} & \mathbf{B}_E & \mathbf{E}_{\text{CAV}, E} \\ \mathbf{K}_{\text{IE}} & \mathbf{K}_{\text{II}} & \mathbf{B}_I & \mathbf{0} \\ \mathbf{C}_E & \mathbf{C}_I & \mathbf{D}_E & \mathbf{0} \\ \mathbf{F}_{\text{CAV}, E} & \mathbf{F}_{\text{CAV}, I} & \mathbf{0} & \mathbf{G}_{\text{CAV}} \end{pmatrix} \begin{pmatrix} \Delta \underline{u}_E \\ \Delta \underline{u}_I \\ \Delta \underline{p}_E \\ \Delta \underline{p}_{\text{CAV}} \end{pmatrix} = \begin{pmatrix} -\underline{R}_{\text{vol}, E} - \underline{R}_{\Gamma, \text{vol}, E} \\ -\underline{R}_{\text{vol}, I} \\ -\underline{R}_{\text{inc}, E} \\ -\underline{R}_{\text{CAV}, E} \end{pmatrix}.$$

Static condensation of all interior degrees of freedom leads to

$$\underbrace{\begin{pmatrix} \widetilde{\mathbf{K}} & \widetilde{\mathbf{B}} & \mathbf{E}_{\text{CAV}, E} \\ \widetilde{\mathbf{C}} & \widetilde{\mathbf{D}} & \mathbf{0} \\ \widetilde{\mathbf{F}}_{\text{CAV}} & \widetilde{\mathbf{H}}_{\text{CAV}} & \mathbf{G}_{\text{CAV}} \end{pmatrix}}_{:=\widetilde{\mathbf{A}}} \begin{pmatrix} \Delta \underline{u}_E \\ \Delta \underline{p}_E \\ \Delta \underline{p}_{\text{CAV}} \end{pmatrix} + \underbrace{\begin{pmatrix} \widetilde{\mathbf{K}}_\Gamma & \widetilde{\mathbf{B}}_\Gamma & \mathbf{0} \\ \mathbf{0} & \mathbf{0} & \mathbf{0} \\ \mathbf{0} & \mathbf{0} & \mathbf{0} \end{pmatrix}}_{:=\widetilde{\mathbf{A}}_\Gamma} \begin{pmatrix} \Delta \underline{u}_E \\ \Delta \underline{p}_E \\ \Delta \underline{p}_{\text{CAV}} \end{pmatrix} = \underbrace{\begin{pmatrix} -\widetilde{\underline{R}}_{\text{vol}} \\ -\widetilde{\underline{R}}_{\text{inc}} \\ \widetilde{\underline{R}}_{\text{CAV}} \end{pmatrix}}_{:=\underline{\mathbf{R}}} + \underbrace{\begin{pmatrix} -\widetilde{\underline{R}}_{\Gamma, \text{vol}} \\ \underline{\mathbf{0}} \\ \underline{\mathbf{0}} \end{pmatrix}}_{:=\underline{\mathbf{R}}_\Gamma},$$

where

$$\begin{aligned} \widetilde{\mathbf{F}}_{\text{CAV}} &:= \mathbf{F}_{\text{CAV}, E} - \mathbf{F}_{\text{CAV}, I} \mathbf{K}_{\text{II}}^{-1} \mathbf{K}_{\text{IE}}, \\ \widetilde{\mathbf{H}}_{\text{CAV}} &:= -\mathbf{F}_{\text{CAV}, I} \mathbf{K}_{\text{II}}^{-1} \mathbf{B}_I, \\ \widetilde{\underline{R}}_{\text{CAV}} &:= \underline{R}_{\text{CAV}} - \mathbf{F}_{\text{CAV}, I} \mathbf{K}_{\text{II}}^{-1} \underline{R}_{\text{vol}, I} \end{aligned}$$

## Appendix C. Tensor calculus

We use the following results from tensor calculus, for more details we refer to, e.g., [108, 109].

$$\begin{aligned} \frac{\partial \overline{\mathbf{C}}}{\partial \mathbf{C}} &= J^{-\frac{2}{3}} \mathbb{P} = J^{-\frac{2}{3}} \left( \mathbb{I} - \frac{1}{3} \mathbf{C}^{-1} \otimes \mathbf{C} \right), \\ \frac{\partial \mathbf{C}^{-1}}{\partial \mathbf{C}} &= -\mathbf{C}^{-1} \odot \mathbf{C}^{-1}, \\ (\mathbf{A} \odot \mathbf{A})_{ijkl} &:= \frac{1}{2} (A_{ik} A_{jl} + A_{il} A_{jk}). \end{aligned}$$

For symmetric  $\mathbf{A}$  it holds

$$\mathbb{P} : \mathbf{A} = \text{Dev}(\mathbf{A}) = \mathbf{A} - \frac{1}{3} (\mathbf{A} : \mathbf{C}) \mathbf{C}^{-1}.$$

The isochoric part of the second Piola–Kirchhoff stress tensor as well as the isochoric part of the fourth order elasticity tensor are given as

$$\mathbf{S}_{\text{isc}} := 2 \frac{\partial \bar{\Psi}(\bar{\mathbf{C}})}{\partial \bar{\mathbf{C}}} = J^{-\frac{2}{3}} \text{Dev}(\bar{\mathbf{S}}), \quad (\text{C.1})$$

$$\bar{\mathbf{S}} := 2 \frac{\partial \bar{\Psi}(\bar{\mathbf{C}})}{\partial \bar{\mathbf{C}}},$$

$$\mathbb{C}_{\text{isc}} := 4 \frac{\partial \bar{\Psi}(\bar{\mathbf{C}})}{\partial \bar{\mathbf{C}} \partial \bar{\mathbf{C}}} = J^{-\frac{4}{3}} \mathbb{P} \bar{\mathbb{C}} \mathbb{P}^\top + J^{-\frac{2}{3}} \frac{2}{3} \text{tr}(\bar{\mathbf{C}} \bar{\mathbf{S}}) \tilde{\mathbb{P}} - \frac{4}{3} \mathbf{S}_{\text{isc}} \overset{\text{S}}{\otimes} \mathbf{C}^{-1}, \quad (\text{C.2})$$

$$\bar{\mathbb{C}} := 4 \frac{\partial \bar{\Psi}(\bar{\mathbf{C}})}{\partial \bar{\mathbf{C}} \partial \bar{\mathbf{C}}},$$

$$\tilde{\mathbb{P}} := \mathbf{C}^{-1} \odot \mathbf{C}^{-1} - \frac{1}{3} \mathbf{C}^{-1} \otimes \mathbf{C}^{-1},$$

$$\mathbf{A} \overset{\text{S}}{\otimes} \mathbf{B} := \frac{1}{2} (\mathbf{A} \otimes \mathbf{B} + \mathbf{B} \otimes \mathbf{A}).$$